# Chapter 2
# Piezoelectric Response at Nanoscale

**Jin Zhang and Shaker A. Meguid**

**Abstract** Considerable efforts were invested to study the piezoelectricity at the nanoscale, which serves as a physical basis for a wide range of smart nanodevices and nanoelectronics. This chapter reviews the recent progress in characterizing the effective piezoelectric property in a nanoworld and the influence of the piezoelectric effect on the mechanical responses of nanoscale structures. Extremely strong piezoelectric responses of piezoelectric nanomaterials were reported in experiments, and the size dependence was observed in atomistic simulations. Attempts were also made to reveal the physics behind these unique features, but the universal theory has not yet been established. Among the proposed mechanisms, the theory of surface piezoelectricity is widely accepted and thus used to derive two effective piezoelectric coefficients (EPCs) for investigating the effect of piezoelectricity on (1) stress or strain and (2) the effective elastic moduli of piezoelectric nanomaterials. The EPCs are found to be size-dependent and also deformation-selective. The obtained results also show that at the nanoscale the surface piezoelectricity can enhance the piezoelectric potential of nanostructures when subjected to a static deformation. In addition, the intrinsic loss of oscillating piezoelectric nanostructures can be mitigated through the piezoelectric effect at the nanoscale.

## 2.1 Introduction

The discovery of advanced nanomaterials has greatly accelerated the development of nanoscience and nanotechnology. Among these nanomaterials are the family of carbon nanomaterials (Kroto et al. 1985; Iijima 1991; Ebbesen and Ajayan 1992; Geim and Novoselov 2007) and that of piezoelectric nanomaterials (PNs) (Wang 2009; Faucher et al. 2009; Smith et al. 2008; Dunn 2003). In particular, the last decade has witnessed increasing interest in PNs, such as nanoscale zinc oxide (ZnO) (Wang 2009), gallium nitride (GaN) (Faucher et al. 2009), barium titanate (BaTiO$_3$) (Smith et al. 2008), and lead zirconate titanate (PZT) (Dunn 2003). These

J. Zhang • S.A. Meguid (✉)

Mechanics and Aerospace Design Laboratory, Department of Mechanical and Industrial Engineering, University of Toronto, Toronto, ON, Canada, M5S 3G8
e-mail: jinzhang@mie.utoronto.ca; meguid@mie.utoronto.ca

PNs form different configurations (e.g., nanodots, nanowires, nanofilms, nanorings, and nanotubes) and have great potential for constructing a wide range of smart piezoelectronic nanosystems, e.g., piezoelectric nanoresonators, nanosensors/actuators, nanogenerators, and nanoelectromechanical systems (Wang 2009; Faucher et al. 2009; Smith et al. 2008; Dunn 2003), which are highly expected to excite ground-breaking innovations in the twenty-first century. Nano-piezoelectricity thus has become a current topic of great interest in recent research (Zhao et al. 2004; Fan et al. 2006; Wang et al. 2006b; Zhu et al. 2008; Bdikin et al. 2010; Espinosa et al. 2012; Fang et al. 2013; Zhang et al. 2014; Xiang et al. 2006; Li et al. 2007; Dai et al. 2010, 2011; Momeni et al. 2012; Momeni and Attariani 2014).

Until now, experimental techniques (Zhao et al. 2004; Fan et al. 2006; Wang et al. 2006b; Zhu et al. 2008; Bdikin et al. 2010; Espinosa et al. 2012; Fang et al. 2013; Zhang et al. 2014) and atomistic simulations (Espinosa et al. 2012; Fang et al. 2013; Zhang et al. 2014; Xiang et al. 2006; Li et al. 2007; Dai et al. 2010, 2011; Momeni et al. 2012; Momeni and Attariani 2014) have been utilized to measure the effective piezoelectric coefficients (EPCs) and examine their size dependence for different sizes and configurations of PNs. Various physical mechanisms were proposed, and especially the theory of surface piezoelectricity (Zhang et al. 2014; Zhang 2014; Zhang and Meguid 2015a, b) was established to interpret the existing data at the nanoscale. However, large discrepancy remains among these studies. For example, EPCs obtained for ZnO nanocrystals differ by up to orders of magnitude and exhibit the size dependence qualitatively different from one another. Specifically, existing piezoelectric measurement was focused on the EPCs describing the electric field-stress relation in the constitutive equations of PNs. The ones characterizing the effect of piezoelectricity on the effective elastic moduli (EEM) of PNs as nanostructures were never considered although they may be of significance for PNs as engineering nanostructures. This situation as it currently stands indeed provides an impulsion to summarize the latest developments, capture the major issues that need to be resolved, and identify the future direction in studying nanoscale piezoelectricity. In addition, further study of the EPCs of PNs by considering both the electric field-stress relation and the electromechanical coupling is essential for the development of PNs and their smart nanosystems.

To achieve these goals, we present this review of the latest developments of nano-piezoelectricity and the derivation of size-dependent and deformation-selective EPCs. The materials are organized as follows: First, a critical review was conducted in Sect. 2.2 regarding the experimental measurements of EPCs and atomistic simulations on the size dependence of EPCs for different configurations of PNs. In Sect. 2.3 we summarized the physical mechanisms proposed in earlier studies for the interpretation of the unique behavior of EPCs. Particular attention was placed on the investigation of the effect of surface piezoelectricity of PNs. Analytical models were derived in Sect. 2.4 for the EPCs and EEM of PNs. Two types of EPCs were obtained in this section reflecting the electric field-stress relation and the electromechanical coupling of PNs. The importance of two EPCs was also evaluated for existing PNs. The influence of the nanoscale piezoelectricity on the mechanical responses (statics and dynamics) of piezoelectric nanostructures was discussed in Sect. 2.5. Finally, the conclusion remarks were given in Sect. 2.6.

## 2.2    Measurement of Nano-piezoelectricity

ZnO nanocrystal exhibits the strongest piezoelectric effect among the tetrahedrally bonded semiconductors, which thus makes it the most studied PNs in the literature (Wang 2009). Throughout the paper, we shall mainly focus our attention on the piezoelectric characterization of ZnO nanocrystals. In 2004 the first piezoelectric measurement of nanoscale ZnO was reported by Zhao et al. (2004) where the piezoelectric force microscope (PFM) was employed to excite the local transverse vibration (the amplitude $A_f$) on the ZnO nanobelts (tens of nanometers in thickness) by applying AC voltage (the amplitude $U_f$) in the thickness direction. The effective $e_{33}$ calculated by $e_{33} = A_f/U_f$ was found to increase from 14.3 to 26.7 pm/V while the driving vibration frequency significantly decreased from 150 to 30 kHz. In other words, obtained $e_{33}$ was found to be frequency-dependent and 40–160 % greater than that of bulk ZnO. Four years later, Zhu et al. (2008) measured $e_{33}$ of ZnO nanowires of diameter ~230 nm using a nanoelectromechanical oscillating system. Their study reported the value of $e_{33} = 3 - 12$  nm/V along the $c$-axis [0001] using $e_{33} = \Delta l/V_{\text{sd}}^{\text{bias}}$, where $V_{\text{sd}}^{\text{bias}}$ is a DC bias voltage applied in the axial direction and $\Delta l$ is the axial extension due to $V_{\text{sd}}^{\text{bias}}$. These values are found to be two to three orders of magnitude greater than the bulk value and those reported for ZnO nanobelts by Zhao et al. (2004). In addition, the giant $e_{33}$ up to 100 pm/V was also achieved by Wang et al. (2006b) for the ZnO nanofilms of thickness ~200 nm doped with ferroelectric vanadium. This value is lower than those reported by Zhu et al. (2008) but still around an order of magnitude greater than the bulk value. The study by Zhao et al. (2004) indicated the rising of EPC with decreasing deriving frequency, and it was attributed to the pinning of spontaneous polarization or imperfect electrical contacts at high frequency. Based on this frequency dependency, the DC bias voltage was thought to be responsible for the extreme value of $e_{33}$ reported by Zhu et al. (2008). Wang et al. (2006b) obtained the giant $e_{33}$, and they attributed this to the switchable spontaneous polarization induced by voltage dopants and the accompanying relatively high permittivity. In contrast to the observations in Zhao et al. (2004), Wang et al. (2006b), and Zhu et al. (2008), $e_{33}$ measured for large ZnO nanopillar (300 nm in diameter and 2 mm in height) in Fan et al. (2006) was around 7.5 pm/V, which was lower than the bulk value. In early studies (Zhao et al. 2004; Fan et al. 2006; Wang et al. 2006b; Zhu et al. 2008), piezoelectric measurement was centered on the ZnO single nanocrystalline. The characterization of the polycrystalline at the nanoscale was not reported until 2010, where the EPCs were measured for the polycrystalline ZnO nanofilms (around 200 nm in thickness and 2 μm in length) based on PFM (Bdikin et al. 2010). The obtained effective value of $e_{33}$ is found to be 12 pm/V, almost the same as the accepted bulk value.

   As reviewed above, EPCs were measured for individual PNs in experiments, but the possible size dependence of EPCs have not yet been investigated experimentally. This is probably due to lack of suitable techniques to control the geometric size of synthesized PNs. To circumvent this hurdle, theoretical studies were performed to calculate the EPC for a group of ZnO nanofilms and nanowires

where the geometric size varies monotonically. Xiang et al. (2006) conducted a density functional study of ZnO nanowires with diameter up to 2.8 nm. In their study, the atomic averaged effective $e_{33}$ is defined as $e_{33} = (V_{\mathrm{scell}}/N)dP/d\varepsilon$ for one-dimensional nanowires, where $\varepsilon$ is the axial compression or tension, $P$ is the polarization induced by $\varepsilon$, $V_{\mathrm{scell}}$ is the volume, and $N$ represents the number of atoms in the supercell. It was found that the effective $e_{33}$ exhibits a significant but nonmonotonic diameter dependence, i.e., with the increasing diameter, $e_{33}$ first decreases to reach its minimum value, then rises, and finally stabilizes when the diameter exceeds 2.8 nm. Here the obtained $e_{33}$ falls in the range 1837–2025 (unit: $10^{-16}$ μCA/ion), which is 20–40 % greater than that of the bulk ZnO. Likewise, density functional theory (DFT) was used by Li et al. (2007) to calculate the effective $e_{33}$ for ZnO nanofilms of a thickness ($h$) up to 2.9 nm. They expressed effective $e_{33}$ as $(\partial P_3/\partial \varepsilon_3)_u + (\partial P_3/\partial u)_\varepsilon (du/d\varepsilon_3)$, where $\varepsilon_3$ and $P_3$ are the strain and polarization in the $c$-axis, respectively, and $u$ is the internal parameter. In this expression, the contributions to the piezoelectric polarization from both the clamped ion and the internal strain have been considered. The results showed that the effective $e_{33}$ increases monotonically with increasing thickness. It becomes greater than the bulk value only when the value of $h$ exceeds 2.4 nm. At the maximum thickness of $h = 2.9$ nm studied, $e_{33}$ was found to be increased by 11 % in comparison to the bulk value. Beyond this limit, the authors expected that $e_{33}$ would further increase to the maximum value and then decrease with increasing $h$ to approach the bulk value at large $h$. This again suggested a nonmonotonic dependence of $e_{33}$ on the feature size of the ZnO nanofilms.

So far, in the existing works, the first-principle calculation remains computationally expensive. Thus, measurements based on this technique (Xiang et al. 2006; Li et al. 2007) are limited to very small ZnO nanocrystal, e.g., feature size less than 2.8 nm (Xiang et al. 2006) and 2.9 nm (Li et al. 2007). To further improve the efficiency and expand the scope of the study, Dai et al. (2010; 2011), Momeni et al. (2012), and Momeni and Attariani (2014) computed the EPC of ZnO nanofilms/nanowires by utilizing molecular dynamics simulations (MDS) based on the empirical core-shell potential. This more efficient technique enabled the authors to consider the nanofilms/nanowires with the thickness up to 10 nm (Dai et al. 2011). The maximum size that can be handled by MDS, however, is still very small as compared with the feature size of synthesized PNs that is of the order of tens to hundreds of nanometers (Zhao et al. 2004; Fan et al. 2006; Wang et al. 2006b; Zhu et al. 2008; Bdikin et al. 2010). A study by Dai et al. (2011) reveals that the magnitudes of the effective $e_{33}$ and $e_{31}$ increase monotonically with increasing thickness $h$ and approach the bulk values gradually at large thickness, $h \geq 10$ nm. As compared with the DFT studies, the MDS predicted the small magnitude and qualitatively different size dependence of the EPC (Dai et al. 2010; Dai et al. 2011; Momeni et al. 2012; Momeni and Attariani 2014). In particular, the magnitudes of the MDS results are always found to be lower than the bulk values.

To show the large scattering of the obtained results, we have summarized the aforementioned experimental and atomistic simulations on (undoped) single ZnO nanocrystal (see Table 2.1). Note that the strong piezoelectric response was

**Table 2.1** Effective piezoelectric coefficients measured for (undoped) single-crystalline ZnO nanofilms and nanowires in exiting experiments and atomistic simulations

| | Nanowires (diameter $d$ or thickness $h$) | | | | Nanofilms (thickness $h$) | | |
|---|---|---|---|---|---|---|---|
| $d$ or $h$ | ~230 nm | ~230 nm | 0.3–2.8 nm | Tens nm | 0.48–2.9 nm | 0.48–2.4 nm | 1.2–9.6 nm |
| $e_{33}$ | ~7.5 (pm/V) | 3–12 (nm/V) | 1837–2025 ($10^{-16}$ µCA/ion) | 14.3–26.7 (pm/V) | 0.5–1.4 (C/m$^2$) | 0.28–1.17 C/m$^2$ | 0.3–1.2 (C/m$^2$) |
| | 374.6–1498.5 (C/m$^2$) | | 1.56–1.73 (C/m$^2$) | 1.79–3.33 (C/m$^2$) | | | |
| $e_{31}$ | | | | | | −0.2 to −0.5 (C/m$^2$) | −0.1 to −0.5 (C/m$^2$) |
| Method | Exp. | Exp. | DFT | Exp. | DFT | DFT | MDS |
| Ref. | Fan et al. (2006) | Zhu et al. (2008) | Xiang et al. (2006) | Zhao et al. (2004) | Li et al. (2007) | Dai et al. (2011) | |

reported in the experiments (Zhao et al. 2004; Fan et al. 2006; Zhu et al. 2008) and DFT studies (Xiang et al. 2006; Li et al. 2007; Dai et al. 2011), where the obtained values of $e_{33}$ were found to be larger than the bulk value. In Zhao et al. (2004), the enhanced piezoelectric response was partially attributed to the perfect single crystallinity and the low density of defects at the nanoscale. This theory, to some extent, is confirmed by the fact that $e_{33}$ of the polycrystalline ZnO nanofilms is almost the same as the bulk value (Bdikin et al. 2010) and also in accordance with Fan et al. (2006) where the authors believed that small $e_{33}$ (smaller than the bulk value) obtained might be a result of relatively high density of defects in the large ZnO films. The free boundary conditions on the lateral surface of nanowires or nanofilms (Zhao et al. 2004; Xiang et al. 2006) were also considered as a physical origin leading to the strong piezoelectric response at the nanoscale, i.e., the free relaxation of the surface atoms along the lateral direction of nanofilms/nanowires would lead to an increase of the strain, which, in turn, yields an effective $e_{33} = e_{33}^b - \nu e_{13}^b > e_{33}^b$ where $\nu$ (>0) is Poisson's ratio and $e_{13}^b$ (<0) and $e_{33}^b$ are piezoelectric coefficients of bulk ZnO. However, the small $e_{33}$ of the polycrystalline ZnO nanofilms indicates that the perfect single crystallinity is more important in determining the piezoelectric effect of ZnO nanocrystal (Bdikin et al. 2010). Moreover, as mentioned before the atomistic simulations in Li et al. (2007) and Dai et al. (2011) predicted weak piezoelectric responses for the perfect ZnO single nanocrystal (i.e., no defects) with the relaxation of surface atoms, which can also be observed from Table 2.1. Obviously, the small EPCs obtained in these simulations cannot be understood based on the physical mechanisms proposed above. Thus, further efforts were made to reveal the physics behind the unique piezoelectric effect at the nanoscale. Following this, the effect of the surface piezoelectricity was identified as one of the major factors that would exert significant influence on the electromechanical behavior of PNs (Dai et al. 2011; Miller and Shenoy 2000; Wang and Feng 2009, 2010; Liu and Rajapakse 2010; Assadi et al. 2010; Assadi and Farshi 2010; Huang and Yu 2006; Yan and Jiang 2010, 2011; Li et al. 2011; Zhang and Wang 2012; Zhang et al. 2012a, b).

## 2.3   Effect of Piezoelectric Surface Layer

It is understood that the miniaturization of materials into the nanoscale significantly increases their surface-to-volume ratio and, thus, substantially enhances the effect of thin surface layers, where atoms experience an environment different than that in the inner section. As reviewed above, one of the surface effects, i.e., the free relaxation of the surface atoms in lateral direction, was thought to be responsible for the enhanced piezoelectric effect at the nanoscale (Zhao et al. 2004; Xiang et al. 2006). In addition to the less constrained atoms, the surface layer also experiences structural changes (e.g., the change in atomic bond length) relative to the bulk materials at the inner sections. In general, these alterations lead to nonzero
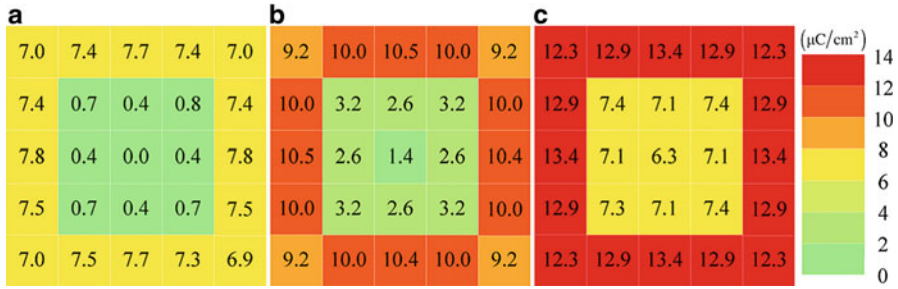
**Fig. 2.1** Evolution of axial polarization distribution along the cross section of a BaTiO$_3$ nanowire under different axial strains. (**a**) $-0.5\%$ strain, (**b**) $0.0\%$ strain, and (**c**) $0.5\%$ strain (Zhang et al. 2010)

residual surface stress and the surface material properties distinct from those of the bulk materials. To examine the effect of elastic surface layer(s), a core-shell or core-surface (CS) model was developed and efficiently utilized to examine the effect of residual surface stress and surface elasticity on the elastic properties and the mechanical responses of nanomaterials (Miller and Shenoy 2000; Wang and Feng 2009, 2010; Liu and Rajapakse 2010; Assadi et al. 2010; Assadi and Farshi 2010). In the CS model, nanomaterials are treated as equivalent composite materials consisting of the bulk material wrapped by a two-dimensional (2D) surface layer.

The "core-surface" concept was extended by Huang and Yu (2006) to evaluate the effect of piezoelectric surface on the structural responses of PNs. Along with the surface residual stress and surface elasticity, the surface piezoelectricity was considered for the first time in the analysis of PNs. The significant influence of surface piezoelectricity was further confirmed based on ab initio and MDS studies (Zhang et al. 2009, 2010). For example, the distributions of polarization due to strain were obtained in Zhang et al. (2010) for a 2 nm thick BaTiO$_3$ nanowire. As shown in Fig. 2.1, the results of Zhang et al. (2010) indicated that the strain-induced polarization on the surface is greater than that found in the core (bulk) section. Motivated by the study of Huang and Yu (2006), Yan and Jiang (2010, 2011) and Li et al. (2011) incorporated the surface piezoelectricity into the CS beam model and studied the bending, vibration, and buckling of one-dimensional (1D) piezoelectric nanowires and nanofilms. Most recently, a sandwich-plate model was developed based on the "core-surface" concept to study the static and dynamic behaviors of 2D piezoelectric nanofilms (Zhang and Wang 2012; Zhang et al. 2012a, b). The influence of the surface piezoelectricity on the EPCs was also discussed briefly in the works of Zhang and Wang (2012) and Zhang et al. (2012a, b).

A general theoretical framework of surface piezoelectricity was formulated by Shen and Hu (2010) for PNs. Consistent with the existing piezoelectric CS models, they stated that the total internal energy density ($W$) consists of the surface energy density ($U_s$) and the energy density of the core section ($U_b$). As a result, the piezoelectricity of both the surface layer and the core section contributes to the

effective piezoelectric properties or the EPCs of PNs. This theory of surface piezoelectricity enabled Dai et al. (2011) to conduct a comprehensive study on the effect of piezoelectric surface on EPCs. Based on $W = U_s/h + U_b$, they derived the analytical formulae for the EPCs ($e_{ij3}^{\text{eff}}$) of the nanofilms with thickness $h$ (Dai et al. 2011):

$$e_{ij3}^{\text{eff}} = e_{ij3}^b + n \frac{e_{ij3}^s}{h} \tag{2.1}$$

where $e_{ij3}^b$ and $e_{ij3}^s$ are the piezoelectric coefficients of the inner bulk material and 2D surface layer, respectively, and $n$ denotes the number of the contributing surfaces. It is interesting to see that the MDS and DFT simulations in Li et al. (2007) and Dai et al. (2011) were well fitted into Eq. (2.1) with almost constant $e_{ij3}^b$ and $e_{ij3}^s$ for $n = 2$ or 4 and $h$ increasing from 0.3 to 10 nm. For a given $e_{31}^b = -0.59 \, \text{C/m}^2$ and $e_{33}^b = 1.22 \, \text{C/m}^2$ of bulk ZnO, the DFT (or MDS) yields $e_{31}^s = 0.1 \times 10^{-9} \, \text{C/m}$, $\left(0.29 \times 10^{-9} \, \text{C/m}\right)$, and $e_{33}^s = -0.15 \times 10^{-9} \, \text{C/m}$ $\left(-0.29 \times 10^{-9} \, \text{C/m}\right)$ for surface layers of ZnO nanofilms. In these studies, the EPCs were also calculated for BaTiO$_3$ and SrTiO$_3$ nanofilms and similar size dependence was also achieved. These results, to a large extent, confirm that the size-dependent EPCs obtained for the PNs attributed to the surface piezoelectricity (Dai et al. 2011). In other words, the piezoelectric CS model can be used for the interpretation of the atomistic simulations on relatively large PNs studied in Dai et al. (2011). Furthermore, it is noted that the surface layer and the bulk materials of ZnO exhibit reverse piezoelectric effects characterized by the piezoelectric coefficients of opposite signs. Thus, the surface piezoelectricity reduces the overall piezoelectric effect of ZnO nanocrystals and leads to the EPCs lower than the bulk values. This is in contrast to the effect of free relaxations of the surface atoms, which, as argued in Zhao et al. (2004) and Xiang et al. (2006), would enhance the resultant piezoelectric effect. We believe that the above two effects of the surface layers were considered naturally in the DFT and MDS studies (Dai et al. 2011). Thus, the low EPCs suggest that the effect of surface piezoelectricity could be even stronger than that of free relaxation of the surface atoms.

On the other hand, the theory of surface piezoelectricity (see Eq. (2.1)) is unable to explain the enhancement of piezoelectric response observed in the experiments (Zhao et al. 2004; Zhu et al. 2008; Bdikin et al. 2010) and earlier atomistic simulations (Xiang et al. 2006; Li et al. 2007) for ZnO nanocrystal. It thus still remains a big challenge to develop a universal theory that is able to account for the large scattering of the EPCs summarized in Table 2.1 and the different size dependence predicted in the simulations (Xiang et al. 2006; Li et al. 2007; Dai et al. 2011). The current authors believe that, in addition to the uncertainty in the experiments and the discrepancy in the simulation theories, the difference among the existing studies may be due to the fact that multifactors instead of single factor influence the piezoelectric responses of PNs. Specifically, in different cases, e.g., at distinct size scale, the key factor may switch from one to another. For example, as

far as very thin PNs (e.g., the feature size is of the order of 1 nm) are concerned with the quantum effect may be predominant over the surface effects. The change of the crystal constant of such thin PNs with their geometric size may also affect their EPCs significantly (Xiang et al. 2006). The effect of these factors, however, is negligible for relatively large PNs (e.g., the feature size of the order of 10 nm) where the surface piezoelectricity dominates. Moreover, for synthesized PNs with geometric size of up to hundred nanometers, the surface effect should also decline as the surface energy decreases at large size. The exceptional piezoelectric effect of synthesized PNs (Zhao et al. 2004; Zhu et al. 2008) is likely due to the specific microstructures of the tested samples, the boundary conditions enforced in the experiments, as well as other factors in the experimental setups due to some unknown physical mechanisms. Indeed, great efforts are required to further advance the physics of the piezoelectricity in a nanoscale world.

## 2.4  Piezoelectricity of Nanostructures

Evidently the continuous attempts to estimate the size-dependent EPCs for PNs are crucial for the design of the PN-based smart nanodevices and nanoelectromechanical systems. Here, it should be emphasized that when put into practical use, PNs serve as not only materials characterized by material constants but also structures (e.g., beams, plates, or cylinders) which are able to sustain different external loadings, e.g., extension, bending, and torsion. As reported previously, in the latter case, the nanostructures may exhibit effective material properties depending on the deformation patterns (or loading conditions). The typical examples are the loading condition-dependent Young's modulus of carbon nanotubes (Huang et al. 2006) and ZnO nanowires (He et al. 2009; Xu et al. 2010). Nevertheless, in all existing theoretical and experimental measurement of EPCs, effective $e_{33}$ and $e_{31}$ were extracted by considering the uniform normal deformation (stresses) generated by an electric field (voltage) or vice versa. Bending or torsion associated with nonuniform deformation (stresses) has never been used. The EPCs obtained in this scenario are the effective material constants relating an electric field to the stresses (stains) in the constitutive relations. The possible loading condition or deformation dependence of EPCs and its influence on the EEM of PNs however have not received enough attention so far.

In fact, as pointed out in Zhang and Wang (2012), Zhang et al. (2012a, b), and Yan and Jiang (2010), (2011), the piezoelectricity of an engineering structure affects its structural responses not only by the voltage ($V$)-induced stresses (strains) due to the converse piezoelectric effect but also via the electromechanical coupling that changes the EEM associated with specific structural stiffnesses. Consequently, both effects of the piezoelectricity should be taken into consideration in calculating the EPCs of PNs as nanostructures. In what follows two piezoelectric nanostructures studied in Yan and Jiang (2010), (2011), Zhang and Wang (2012), and Zhang et al. (2012a, b) will be considered herein: (1) the 2D piezoelectric

**Fig. 2.2** Schematic illustrations of (**a**) a piezoelectric rectangular nanofilm, (**b**) a piezoelectric nanobeam with rectangular cross section, and (**c**) a piezoelectric nanobeam with circular cross section subjected to an electric voltage $V$
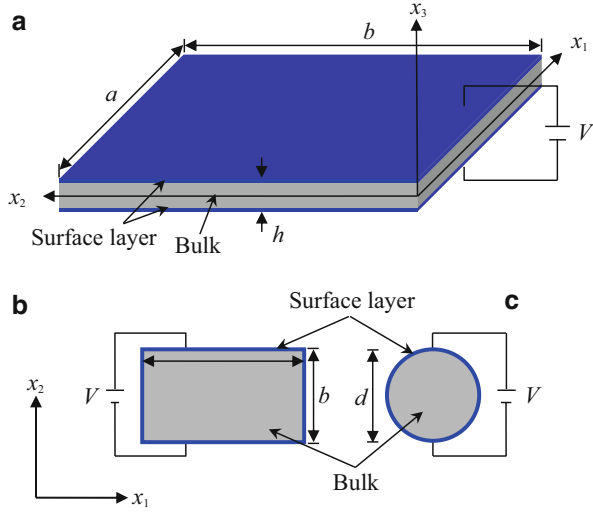
rectangular nanofilms with thickness $h$ and an electric voltage $V$ applied in their thickness direction (Zhang and Wang 2012; Zhang et al. 2012a, b) (Fig. 2.2a) and (2) the 1D piezoelectric nanowires (films) subjected to an electrical voltage $V$ across their cross sections (Yan and Jiang 2010, 2011) (Fig. 2.2b, c). It was shown in Zhang and Wang (2012) and Zhang et al. (2012a, b) that the overall structural responses of the piezoelectric nanofilms are controlled by the membrane stress, $N_{ij}$; the off-plane stiffness, $D_{ijkl}$; and in-plane stiffness, $K_{ijkl}$:

$$N_{ij} = K_{ijkl}\gamma_{kl} + 2\sigma_{ij}^0 + \left( e_{ij3}^b + 2\frac{e_{ij3}^s}{h} \right)V \tag{2.2}$$

$$K_{ijkl} = \left( c_{ijkl} + 2\frac{c_{ijkl}^s}{h} \right)h \tag{2.3}$$

$$D_{ijkl} = \left[ c_{ijkl} + 6\frac{c_{ijkl}^s}{h} + \frac{e_{ij3}^b}{k_{33}}\left( d_{kl3}^b + 6\frac{e_{kl3}^s}{h} \right) \right]\frac{h^3}{12} \tag{2.4}$$

Here $c_{ijkl}^b$ and $c_{ijkl}^s$ are elastic moduli, $e_{ijkl}^b$ and $e_{ijkl}^s$ are piezoelectric constants, and $k_{33}$ is dielectric constant. Superscripts $b$ and $s$ represent the parameters of the bulk material and surface layer, respectively. Subscripts $i$, $j$, $k$, and $l$ are equal to 1 or 2. $\gamma_{kl}$ and $\sigma_{ij}^0$ represent in-plane strain and surface residual stresses, respectively. In addition, Yan and Jiang (2010, 2011) showed that for beam-like piezoelectric nanowires, the structural responses are determined by the applied axial force, $P$; the extensional stiffness, $EA$; and the bending stiffness, $EI$. For the nanowires with rectangular cross section of width $a$ and height $b$ (see Fig. 2.2b), we have (Yan and Jiang 2011)

$$P = EA\varepsilon_0 + \left[2\sigma_{11}^0 + \left(e_{31}^b + 2\frac{e_{31}^s}{b}\right)V\right]a \tag{2.5}$$

$$EA = \left(c_{11}^b + 2\frac{c_{11}^s}{b}\right)ab \tag{2.6}$$

$$EI = \left\{c_{11}^b + \left(\frac{6}{b} + \frac{2}{a}\right)c_{11}^s + \frac{e_{31}}{k_{33}}\left[e_{31}^b + \left(\frac{6}{b} + \frac{2}{a}\right)e_{31}^s\right]\right\}\frac{ab^3}{12} \tag{2.7}$$

Those derived for the nanowires with circular cross section of diameter $d$ (Fig. 2.2c) are as follows (Yan and Jiang 2011):

$$P = EA\varepsilon_0 + \left[2\sigma_{11}^0 + \left(e_{31}^b + \frac{8}{\pi}\frac{e_{31}^s}{d}\right)\frac{\pi}{4}V\right]d \tag{2.8}$$

$$EA = \left(c_{11}^b + \frac{8}{\pi}\frac{c_{11}^s}{d}\right)\frac{\pi d^2}{4} \tag{2.9}$$

$$EI = \left[c_{11}^b + 8\frac{c_{11}^s}{d} + \frac{e_{31}^b}{k_{33}}\left(e_{31}^b + 8\frac{e_{31}^s}{d}\right)\right]\frac{\pi d^4}{64} \tag{2.10}$$

### 2.4.1  Effective Piezoelectric Coefficients $e_{31}^{e1}$ and $e_{31}^{e2}$

Based on Eqs. (2.2) to (2.10), we will first derive $e_{31}^{e1}$ of the PNs considering the contribution of piezoelectricity to the EEM of the PNs. This effect of piezoelectricity has never been considered before in piezoelectric measurement. We shall first obtain the formulae of EEM. In the structural stiffness Eqs. (2.3), (2.4), (2.5), (2.7), (2.9), and (2.10), the coefficients represent the EEM of the nanostructures and thus are tabulated in Table 2.2. As noted in Table 2.2, EEM not only depends on the feature size of the PNs (e.g., the thickness $h$ or the diameter $d$) but also varies with the deformation of the PNs. The origin of these unique features is the surface piezoelectricity and/or surface elasticity, whose effect is inversely proportional to the geometric size of the PNs and turns out to be more significant for the EEM associated with off-plane deformation, e.g., bending or off-plane torsion. It is also noted that the piezoelectricity of the PNs only contributes to $c_{11}$ (note $c_{11} = c_{22}$ for an isotropic material) associated with bending but has no influence on the EEM associated with uniform tension/compression or torsion.

Next, let us calculate $e_{31}^{e1}$ characterizing the electromechanical coupling of the nanostructures, i.e., the effect of piezoelectricity on the EEM. To this end, we shall concentrate on the piezoelectric terms found in the function of $c_{11}^{e1}$ and $c_{11}^{e2}$ (see Table 2.2). First $e_{31}^b[e_{31}^b + (6/h)e_{31}^s]/k_{33}$ can be obtained for the piezoelectric nanoplates (films). At $e_{31}^s = 0$ it reduces to $(e_{31}^b)^2/k_{33}$ providing the effect of

**Table 2.2** Formulae derived for the effective elastic modulus $c_{11}^{e1}$ and $c_{11}^{e2}$, and effective piezoelectric coefficients $e_{31}^{e1}$ and $e_{31}^{e2}$ of piezoelectric nanofilms and nanobeams subjected to various deformations

| | Nanofilms | Nanobeams (rectangular) | Nanobeams (circular) |
|---|---|---|---|
| $c_{11}^{e1}$ | $c_{11}^b + 2\dfrac{c_{11}^s}{h}$ | $c_{11}^b + 2\dfrac{c_{11}^s}{h}$ | $c_{11}^b + \dfrac{8}{\pi d}c_{11}^s$ |
| $c_{11}^{e2}$ | $c_{11}^b + 6\dfrac{c_{11}^s}{h} + \dfrac{e_{31}^b}{k_{33}}\left(e_{31}^b + \dfrac{6}{h}e_{31}^s\right)$ | $c_{11}^b + \left(\dfrac{6}{b}+\dfrac{2}{a}\right)c_{11}^s + \dfrac{e_{31}^b}{k_{33}}\left[e_{31}^b + \left(\dfrac{6}{b}+\dfrac{2}{a}\right)e_{31}^s\right]$ | $c_{11}^b + \dfrac{8}{\pi d}c_{11}^s + \dfrac{e_{31}^b}{k_{33}}\left(e_{31}^b + \dfrac{8}{\pi d}e_{31}^s\right)$ |
| $e_{31}^{e1}$ | $\sqrt{\left(e_{31}^b\right)^2 + \left(\dfrac{6}{h}\right)e_{31}^b e_{31}^s}$ | $\sqrt{\left(e_{31}^b\right)^2 + \left(\dfrac{6}{h}+\dfrac{2}{b}\right)e_{31}^b e_{31}^s}$ | $\sqrt{\left(e_{31}^b\right)^2 + \left(\dfrac{8}{\pi h}\right)e_{31}^b e_{31}^s}$ |
| $e_{31}^{e2}$ | $e_{31}^b + 2\dfrac{e_{31}^s}{h}$ | $e_{31}^b + 2\dfrac{e_{31}^s}{h}$ | $e_{31}^b + \dfrac{8}{\pi h}e_{31}^s$ |

piezoelectricity on $c_{11}$ of classical piezoelectric plates without surface piezoelectricity. Therefore, considering the nanofilms as equivalent classical plates with piezoelectric constant $e_{31}^{e1}$, one can have $\left(e_{31}^{e1}\right)^2 = e_{31}^b\left[e_{31}^b + (6/h)e_{31}^s\right]$ which yields $e_{31}^{e1} = \sqrt{e_{31}^b\left[e_{31}^b + (6/h)e_{31}^s\right]}$. Following a similar procedure, one is able to derive $e_{31}^{e1}$ for the two nanobeams studied here. The results are also shown in Table 2.2.

Subsequently, we shall turn to $e_{31}^{e2}$ characterizing the $V$-induced forces on the piezoelectric nanofilms and nanowires, i.e., the relation between the stresses (deformation) and an electric voltage (field). This is the piezoelectric effect we usually refer to and was considered in previous piezoelectric measurements of PNs (Zhao et al. 2004; Fan et al. 2006; Wang et al. 2006a, b; Zhu et al. 2008; Bdikin et al. 2010; Espinosa et al. 2012; Fang et al. 2013; Zhang et al. 2014). The $V$-induced forces of the PNs extracted from Eqs. (2.2), (2.5), and (2.8) are $\left(e_{ij3}^b + 2e_{ij3}^s/h\right)V$, $\left(e_{31}^b + 2e_{31}^s/b\right)aV$, and $\left[e_{31}^b + (8/\pi)e_{31}^s/d\right]\pi dV/4$, respectively. By assuming $e_{ij3}^s = 0$ the $V$-induced forces of the corresponding macroscopic structures can be achieved as $e_{ij3}^b V$, $e_{31}^b aV$, and $e_{31}^b \pi dV/4$. Subsequently, $e_{31}^{e2}$ of PNs can be easily obtained by equating the $V$-induced forces of PNs to the forces of corresponding macroscopic structures. The results are presented in Table 2.2 in comparison with $e_{31}^{e1}$.

It may be observed from Table 2.2, EPCs of PNs are also size-dependent as a result of the effect of surface piezoelectricity. Such an effect increases with decreasing geometric size of the nanofilms or nanobeams. In particular, it is noted that $e_{31}^{e2}$ achieved for the quasi-2D piezoelectric nanofilms via the voltage-stress relation is identical to Eq. (2.1) (Dai et al. 2011) derived based on the theory of surface piezoelectricity (Zhang et al. 2009). Other formulae in Table 2.2 are reported for the first time in the literature. From Table 2.2 it follows that, in principle, the general form of EPC function does not exist. Thus, a particular form of EPC should be selected for corresponding deformation experienced by the PNs. For example, when uniform tension or compression is concerned, $e_{31}^{e2}$ should be incorporated, whereas $e_{31}^{e1}$ is not required as there is no bending. However, both $e_{31}^{e1}$ and $e_{31}^{e2}$ may be used when more general cases are considered, e.g., the transverse vibration or the buckling of nanofilms and nanobeams, where both bending stiffness and normal prestresses may significantly influence (Yan and Jiang 2010, 2011; Zhang and Wang 2012; Zhang et al. 2012a, b).

## 2.4.2  Importance of Coefficients $\mathbf{e}_{31}^{e1}$ and $\mathbf{e}_{31}^{e2}$

As shown in Sect. 2.4.1, in nano-piezoelectricity theory, there exist two types of EPCs for PNs, i.e., $e_{31}^{e1}$ and $e_{31}^{e2}$, which reflect different physical mechanisms of the piezoelectric effect. It is thus of interest to evaluate (1) the effect of the surface piezoelectricity on the two EPCs and (2) the importance of the two EPCs for
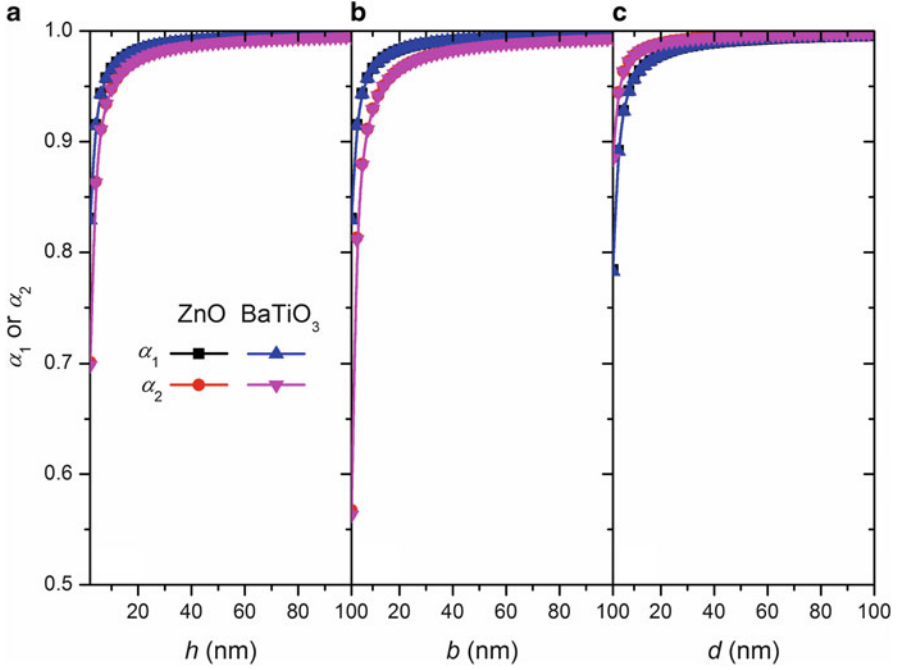
**Fig. 2.3** The ratios $\alpha_1 = e_{31}^{e1}/e_{31}^b$ and $\alpha_2 = e_{31}^{e2}/e_{31}^b$ calculated for ZnO and BaTiO$_3$ (**a**) nanofilms with thickness $h$ (Fig. 2.2a), (**b**) nanowires with rectangular cross section of height $b$ (Fig. 2.2b), and (**c**) nanowire with circular cross section of diameter $d$ (Fig. 2.2c)

**Table 2.3** Material properties of ZnO and BaTiO$_3$ used in Figs. 2.3, 2.4, and 2.5

|  | ZnO | BaTiO$_3$ |
|---|---|---|
| $c_{11}$ (GPa) | 209.7 | 222 |
| $e_{31}^b$ (C/m$^2$) | −0.59 | −4.1 |
| $e_{31}^s$ ($10^{-9}$ C/m) | 0.1 | 0.7 |
| $k_{33}$ (pF/m) | 78.89 | 1142.17 |

$c_{11}$ is the elastic modulus, $e_{31}^b$ and $e_{31}^s$ are the piezoelectric constants for the bulk materials and surface layer, and $k_{33}$ is dielectric constant

existing PNs of different configurations. To achieve the first goal, the ratios $\alpha_1 = e_{31}^{e1}/e_{31}^b$ and $\alpha_2 = e_{31}^{e2}/e_{31}^b$ are calculated in Fig. 2.3 for nanofilms and nanobeams against their feature size. The material properties of ZnO and BaTiO$_3$ considered in Fig. 2.3 are summarized in Table 2.3. It is seen from Fig. 2.3 that $\alpha_1$ and $\alpha_2 < 0.95$, i.e., $e_{31}^{e1}$ and $e_{31}^{e2} < 0.95e_{31}^b$, at the feature size around 10 nm or smaller. Thus, the surface piezoelectricity affects the EPCs of ZnO and BaTiO$_3$ nanocrystal significantly (say, >5 %) when the feature size is of the order of 10 nm. In Fig. 2.3 such an effect increases to 10 % (i.e., $\alpha_1$ and $\alpha_2 < 0.9$ or $e_{31}^{e1}$ and $e_{31}^{e2} < 0.9e_{31}^b$) when the feature size is down to around 5 nm. On the other hand, at the feature size much

larger than 10 nm, the effect of the surface piezoelectricity becomes negligible. These results are found to be in a good agreement with those predicted by Dai et al. (2011).

According to the definition illustrated above, $e_{31}^{e2}$ characterizes the contribution of piezoelectricity to the initial stress on the PNs. The surface residual stress $\sigma^0$ of ~1 N/m (Zhang and Wang 2012; Zhang et al. 2012a, b) is also a part of this initial stress and is identified as a major factor that can substantially affect the structural responses of PNs (Yan and Jiang 2010, 2011; Zhang and Wang 2012; Zhang et al. 2012a, b). Thus, to show the significance of $e_{31}^{e2}$, we computed the ratio $\beta = \sigma/\sigma^0$ in Fig. 2.4 for the same PNs studied in Fig. 2.3. Here $\sigma = e_{31}^{e2}V$ is the V-induced initial stress and $\sigma^0$ (~1 N/m) represents the surface residual stress. Figure 2.4 shows that at low voltage $V = 0.1\text{--}0.5$ V, $\sigma$ is up to 1.2 (BaTiO$_3$) and 2 (ZnO) times that of $\sigma^0$ and will further increase at higher $V$. The importance of $e_{31}^{e2}$ can thus be manifested here as $\sigma$ due to $e_{31}^{e2}$ which can be even greater than $\sigma^0$. Next, the importance of $e_{31}^{e1}$ was evaluated in Fig. 2.5 by calculating the ratio $\gamma = \left(e_{31}^{e1}e_{31}^{e1}/k_{33}\right)/c_{11}$, where $e_{31}^{e1}e_{31}^{e1}/k_{33}$ is the increase of $c_{11}$ (associated with bending in Table 2.2) due to the electromechanical coupling characterized by $e_{31}^{e1}$. Figure 2.5 shows that the increase of the elastic modulus is considerable (~6 %) for ZnO nanocrystal but negligible (~2 %)



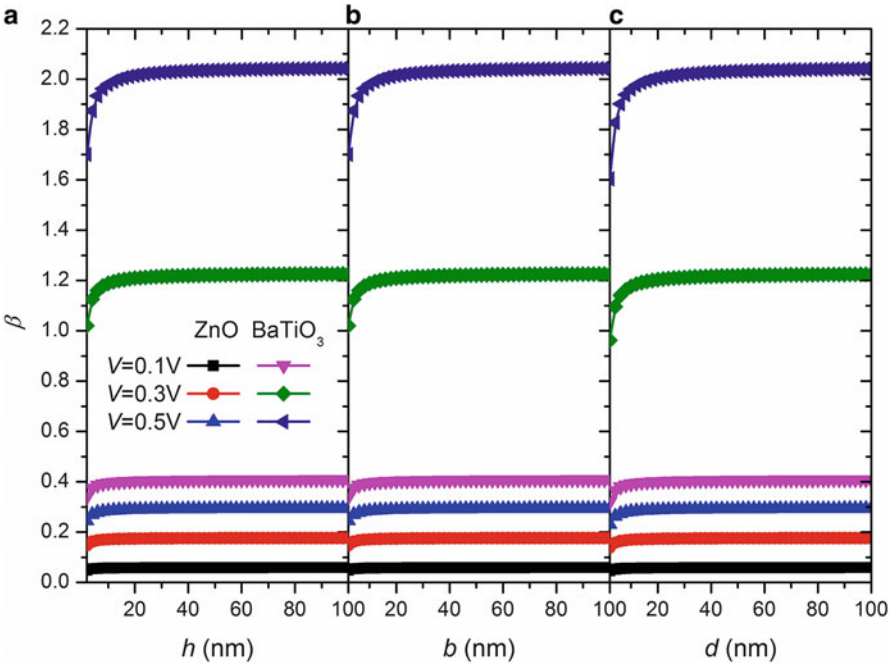**Fig. 2.4** The ratio of $\beta = \sigma/\sigma^0$ calculated for ZnO and BaTiO$_3$ (**a**) nanofilms with thickness $h$ (Fig. 2.2a), (**b**) nanowires with rectangular cross section of height $b$ (Fig. 2.2b), and (**c**) nanowires with circular cross section of diameter $d$ (Fig. 2.2c). Here $e_{31}^{e2}V$ is the stress induced by an electrical voltage $V$ due to $e_{31}^{e2}$ and $\sigma^0$ (~1 N/m) is the residual surface stress
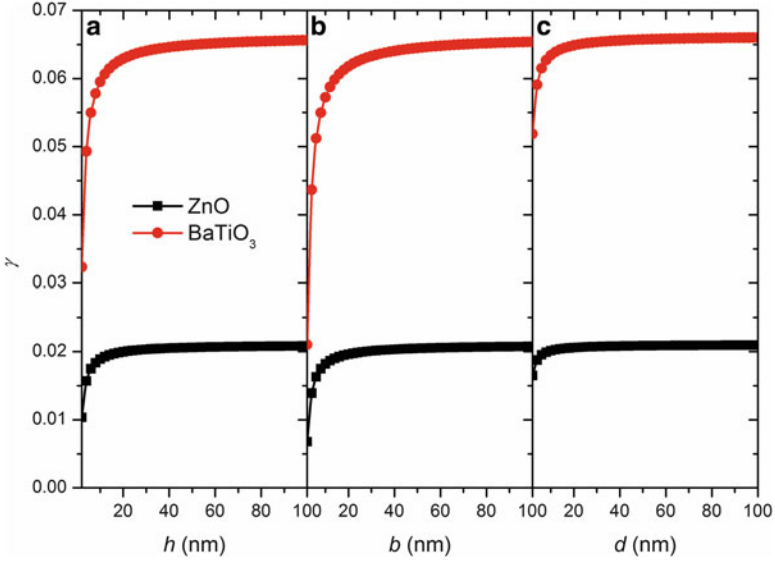
**Fig. 2.5** The ratio $(e_{31}^{e1}e_{31}^{e1}/k_{33})/c_{11}$ calculated for ZnO and BaTiO$_3$ nanofilms with thickness $h$ (Fig. 2.2a), nanowires with rectangular cross section of height $b$ (Fig. 2.2b), and nanowires with circular cross section of diameter $d$ (Fig. 2.2c). Here $e_{31}^{e1}e_{31}^{e1}/k_{33}$ represents the contribution of piezo-electricity to the effective elastic modulus $c_{11}^{e2}$ and $c_{11}$ is the elastic modulus of the bulk materials

for the BaTiO$_3$ nanostructures. Here it is worth noting that in Figs. 2.3, 2.4, and 2.5, the values of piezoelectric constants determined using MDS (Dai et al. 2011) are shown, which are even lower than the bulk values. Nevertheless, the existing experiments (Zhao et al. 2004; Wang et al. 2006a, b; Zhu et al. 2008) showed that the $e_{33}$ of ZnO at the nanoscale can be increased to one to three orders of magnitude greater than the bulk value, by, e.g., doping with ferroelectric vanadium (Wang et al. 2006a, b). In this case, the value of $e_{31}^{e1}$ and $e_{31}^{e2}$ would also increase and thus greatly increase the ratios $\beta = \sigma/\sigma^0$ and $\gamma = \left(e_{31}^{e1}e_{31}^{e1}/k_{33}\right)/c_{11}$. In other words, the EEM (Table 2.2) and $\sigma$ of PNs would rise by orders of magnitude. In these particular cases, both $e_{31}^{e1}$ and $e_{31}^{e2}$ play a critical role in structural responses of PNs and thus have to be taken into consideration in static deformation and vibration and buckling analyses of PNs.

## 2.5   Influence of Piezoelectricity on Mechanical Responses of Nanostructures

In preceding sections we have summarized the measurement of the piezoelectricity at the nanoscale and also compared the piezoelectricity at the nanoscale to that at the macroscale. In this section we will discuss how the nanoscale piezoelectricity

influences the mechanical responses (statics and dynamics) of piezoelectric nanostructures. Specifically, regarding the static behavior, we will study the piezo-electric potential of GaN nanotubes. In terms of the dynamics, we will show the piezoelectric effect on the intrinsic dissipation in oscillating GaN nanobelts.

## 2.5.1 On the Piezoelectric Potential of GaN Nanotubes

### 2.5.1.1 Material Properties of GaN Nanotubes

In this section, MDS were employed to calculate the equivalent elastic, piezoelec-tric, and dielectric properties of GaN nanotubes. In this study, we consider the most common GaN nanotube whose growth direction is along the [001] crystalline direction. The nanotubes have hexagonal cross sections with a sixfold symmetry and lateral surfaces {100} (Han et al. 2000) as shown in Fig. 2.6a. Such shapes have been observed in GaN nanotubes grown by chemical-thermal evaporation (Han et al. 2000). Initially, Ga and N atoms are arrayed in a single-crystalline wurtzite structure with the lattice constants, $a = 3.19$ Å and $c = 5.20$ Å (Bere and Serra



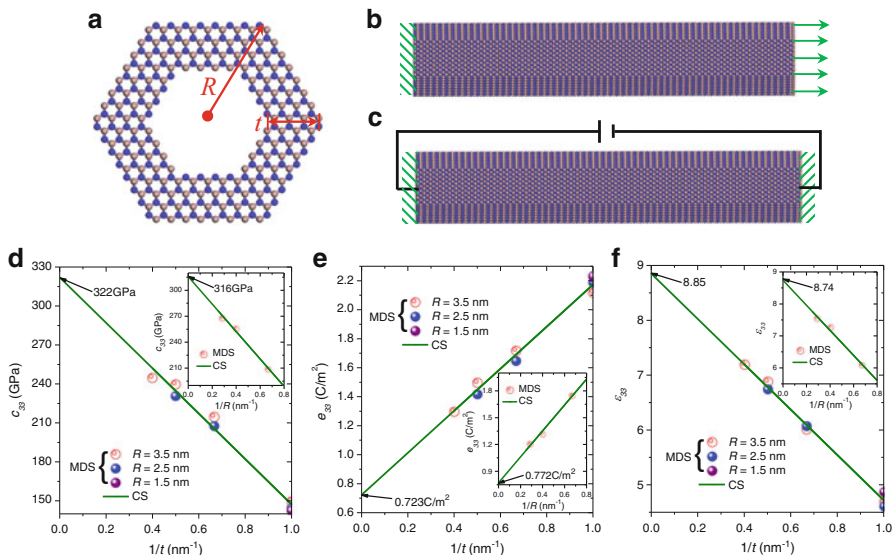**Fig. 2.6** (**a**) Molecular representation of the cross section of a GaN nanotube. The radius is $R$ and the wall thickness is $t$. The simulation setup for the measurement of (**b**) the elastic property, and (**c**) the piezoelectric and dielectric properties of GaN nanotubes. (**d**) The elastic constant $c_{33}$, (**e**) the piezoelectric coefficient $e_{33}$, and (**f**) the dielectric constant $\varepsilon_{33}$ as a function of the inverse of the wall thickness, $1/t$, of the nanotubes with various radii $R$, which are based on MDS and CS model. The insets in (**d**)–(**f**) show the corresponding results for solid GaN nanowire as a function of the inverse of their radius, $1/R$ (Zhang and Meguid 2015a)

2006). The length $L$ of the nanotubes is fixed at 30 nm, whereas the radius $R$ and the wall thickness $t$ of the hexagonal cross section were allowed to change to study the size-dependent material properties of nanotubes.

Classical MDS were conducted in this study, and the NVT ensemble (constant number of particles, volume, and temperature) was employed to update the positions and velocities of the atoms after each time step by using the Nosé-Hoover temperature thermostat (Nosé 1984). The interactions between Ga-Ga, N-N, and Ga-N were described by the Stillinger-Weber (SW) potential (Stillinger and Weber 1985), which contains a two-body term $\varphi_2$ and a three-body term $\varphi_3$, as follows:

$$\varphi_2\left(r_{ij}\right) = A\delta\left(B\left(\frac{r_{ij}}{d}\right)^{-4} - 1\right)\exp\left(\left(\frac{r_{ij}}{d} - r\right)^{-1}\right), \frac{r_{ij}}{d} < r, \qquad (2.11)$$

$$\varphi_2\left(r_{ij}\right) = 0, \frac{r_{ij}}{d} \geq r, \qquad (2.12)$$

$$\varphi_3\left(r_{ij}, r_{ik}, \theta_{ijk}\right) = \delta C\exp\left(\gamma\left(r_{ij} - r\right)^{-1} + \gamma\left(r_{ik} - r\right)^{-1}\right)\left(\cos\theta_{ijk} + \frac{1}{3}\right)^2 \qquad (2.13)$$

Here, subscripts $i$, $j$, and $k$ represent the different atoms in the system; $\delta$ is the cohesive energy of the bond; $d$ is the length unit; $r$ is the cutoff distance; $r_{ij}$ is the length of the bond $ij$; and $\theta_{ijk}$ is the angle formed by the $ji$ and the $jk$ bonds. Other parameters, $A$, $B$, and $C$, are dimensionless fitting parameters adjusted to match the material properties. The values used in this study are taken from Bere and Serra (2006). The SW potentials have been used to reproduce bulk structures and mechanical properties; they have been successfully employed to evaluate the material properties of single-crystal GaN nanowires (Zhang et al. 2013; Zhang 2014; Minary-Jolandan et al. 2012; Wang et al. 2007) and fracture of single-crystal GaN nanotubes (Wang et al. 2006a, 2008). These calculations have demonstrated that the empirical SW potentials for GaN can be employed to study the mechanical behaviors of single-crystal GaN structures. In addition, the potentials can handle dangling bonds, wrong bonds, and excess bonds in bulk GaN very well. Therefore, these potentials are proven to be reliable in characterizing the mechanical responses of GaN nanotubes.

As a quasi-1D nanostructure, the elastic, piezoelectric, and dielectric properties of the GaN nanotubes in the axial direction ($c$-axis) are of major concern and can be, respectively, characterized by the axial elastic constant $c_{33}$, piezoelectric coefficient $e_{33}$, and dielectric constant $k_{33}$. At the beginning of all simulations of these material properties, the equilibrium of the initial structure was achieved corresponding to the lowest energy of the nanotube structure in 100 ps. After the full relaxation, different treatments were applied to calculate the material properties (see Fig. 2.6b, c) and are discussed briefly below. Here all MDS were conducted using the open-source LAMMPS (Plimpton 1995) under room temperature (300 K) and without periodic boundary conditions.

Determination of the Elastic Property

To measure the elastic constant $c_{33}$, one end of the nanotube was pulled along the axial direction while the other end was fixed (Fig. 2.6b). The deformation of the nanotube was then measured by the axial strain $\lambda_3$, which generated a tensile stress $\sigma_3$ in the nanotubes. Here, the tensile stress $\sigma_3$ was taken as the arithmetic mean of the local stresses on all atoms, as follows:

$$\sigma_3 = \frac{1}{N} \sum_{i=1}^{N} \frac{1}{V_i} \left( m_i v_3^i v_3^i + \frac{1}{2} \sum_{j \neq i}^{N} F_3^{ij} r_3^{ij} \right) \tag{2.14}$$

Here $m_i$ is the mass of atom $i$; $v_3^i$ is the velocity component in the axial direction of atom $i$; $F_3^{ij}$ refers to the axial component of the interatomic force between atoms $i$ and $j$; $r_3^{ij}$ is the interatomic distance in the axial direction between atoms $i$ and $j$; $V_i$ refers to the volume of atom $i$, which is assumed as a hard sphere in a closely packed undeformed crystal structure; and $N$ is the number of atoms. For small strain case, i.e., $\lambda_3 \leq 0.01$, the elastic constant $c_{33}$ can be obtained from the slope of the linear $\sigma_3 - \lambda_3$ curve since $c_{33} = \partial \sigma_3 / \partial \lambda_3$ for structure under small deformation.

Determination of the Piezoelectric Property

In the measurement of the piezoelectric coefficient $e_{33}$, we fixed the two ends of the nanotubes. It is worth mentioning that simulation process was conducted after its initial relaxation to avoid prestraining the nanotube structure. Then, an electric field $E_3$ was applied to the nanotubes along the axial direction (see Fig. 2.6c). The external force on ion $i$ due to the electric field can be expressed as $F_i = q_i E_3$, where $q_i$ is the charge on ion $i$. Finally, the nanotube was relaxed again to reach a new equilibrium state. Following that, the stress $\sigma_3$ in the axial direction is calculated based on Eq. (2.12). The piezoelectric coefficient $e_{33}$ can then be calculated as the negative slope of the $\sigma_3 - E_3$ curve, since it is defined as $e_{33} = -\partial \sigma_3 / \partial E_3$ (Zhang et al. 2013).

Determination of the Dielectric Property

The dielectric constant $k_{33}$ can be defined as $k_{33} = k_0(1 + \chi_{33})$ with $\chi_{33} = (\partial P_3 / \partial E_3)/k_0$ being the electric susceptibility of the material (Zhang 2014). Here $k_0$ is the vacuum permittivity and $P_3$ is the axial polarization density. It is noted that the axial polarization $P_3$ is mainly determined by the polarization due to the relative displacement between Ga and N atoms, since the polarization between the nucleus and electron cloud is negligible (Zhang 2014). The axial polarization density vector can thus be further written as $P_3 = \sum_{i=1}^{N} x_3^i q_i / \overline{V}$, where $x_3^i$ is the

coordinate along the axial direction of atom $i$ and $\overline{V}$ is the volume of the nanotube. To obtain $\chi_{33}$ and $k_{33}$, we fixed the two ends of the nanotubes after the initial relaxation and applied an electric field $E_3$ to the nanotube in the axial direction (see Fig. 2.6c). Following this, the nanotube was relaxed again to reach a new equilibrium state. The axial polarization density vector $P_3$ of this new equilibrium state was obtained according to the above definition. Finally, the dielectric constant $k_{33}$ can thus be determined from the slope of the obtained linear $P_3 - E_3$ curve.

The elastic constant $c_{33}$, piezoelectric coefficient $e_{33}$, and relative dielectric constant $\varepsilon_{33}$ ( $\varepsilon_{33} = k_{33}/k_0$ ) obtained from the approaches described above are plotted in Fig. 2.6d–f (solid circles) as a function of the inverse of the wall thickness, $1/t$, of nanotubes with various radii $R$. In addition, based on similar simulation techniques described above, the corresponding results of their solid nanowire counterparts are also measured and presented as insets in Fig. 2.6d–f (solid circles) against the inverse of their radius, $1/R$. It is well known that for the solid nanowire, its cross section is determined based on its radius. As a result, its material properties are generally found to only depend on the nanowire radius due to the small-scale effect (Zhang et al. 2013; Zhang 2014). For example, we can see from the insets of Fig. 2.6d–f that $c_{33}$ and $\varepsilon_{33}$ of the nanowires, respectively, increase by 28 and 23 % as their $R$ increases from 1.5 to 3.5 nm. Similarly, in this process, $e_{33}$ is found to decrease by 30 %. Concerning the nanotube structures, we notice that their cross section is not only characterized by $R$ but also by their wall thickness $t$ (see Fig. 2.6a). From Fig. 2.6d–f, we can observe that in nanotubes, the wall thickness $t$ rather than the radius $R$ becomes the major geometric parameter that dominates their material properties. For instance, when $t = 1.5$ nm, all measured $c_{33}$, $e_{33}$, and $\varepsilon_{33}$ of the nanotubes were found to be around 146 GPa, 2.18 C/m$^2$, and 4.73, respectively, as $R$ increases from 1.5 to 3.5 nm. However, when $R$ is fixed at 3.5 nm, $c_{33}$ and $\varepsilon_{33}$ of the nanotubes increased by 63 and 53 %, respectively, and $e_{33}$ decreased by 39 % as $t$ increases from 1 to 2.5 nm.

### 2.5.1.2 Core-Surface Model

To understand the size-dependent material properties observed in Sect. 2.5.1.1, we will introduce a CS model in this section. It is known that the reduction in the size of materials to the nanoscale increases their surface-to-volume ratio and substantially enhances the influence of thin surface layers, where atoms experience structure reconstruction. In general, the surface reconstruction leads to a distinct surface layer that is different than its bulk. For example, in Fig. 2.7a we have shown the potential energy distribution of the cross section of a GaN nanotube after the full relaxation. Figure 2.7a illustrates that nanotubes usually hold two surfaces (inner and outer surfaces) and note that the potential energy of these two surfaces is almost the same. However, the potential energy of these two surfaces is different from that of their bulk counterpart. In fact, the potential energy of the two surfaces is about 23 % greater than that of their bulk counterpart (see Fig. 2.7a). It is believed that the
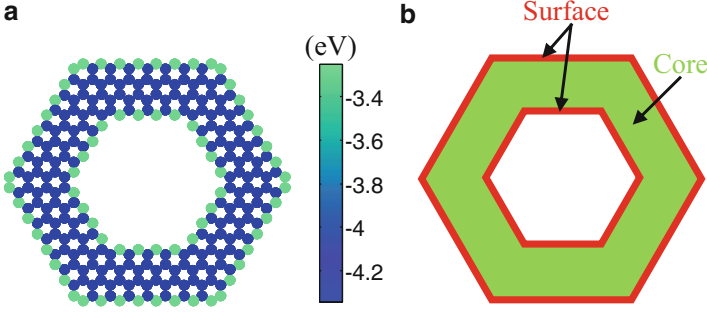
**Fig. 2.7** (**a**) The potential energy distribution of the cross section of the GaN nanotube after the full relaxation. (**b**) An equivalent core-surface model of the GaN nanotube (Zhang and Meguid 2015a)

difference of the physics between the surface layer and the bulk part of the nanostructures results in distinct material properties in layer and bulk and is responsible for the size-dependent material properties observed at the nanoscale (Zhang et al. 2014). Inspired by this idea, a CS model was developed to characterize the size-dependent material properties observed in nanowires (Chen et al. 2006; Xu et al. 2010; Zhang et al. 2013; Zhang 2014; Yang et al. 2012; Yao et al. 2012), where a nanowire is modeled as a composite beam consisting of the core section of the bulk material and the surface layer with two distinct properties. In this section, we will extend the idea of the CS model from the nanowire to the present nanotube structure, which holds two surface layers, as depicted in Fig. 2.7b.

The internal energy density $W$ (incorporating surface contributions) is $W = U^b + 6U^s(2R - t)/S$ for the present nanotube with a hexagonal cross section and $W = U^b + 6U^sR/S$ for its solid nanowire counterpart, where $U^b$ is the bulk internal energy density function and $U^s$ is the surface internal energy density. Here $S$ is the area of the cross section and equals to $3\sqrt{3}(2R - t)t/2$ for the nanotube and $3\sqrt{3}R^2/2$ for the nanowire. Thus, the internal energy density can be rewritten as:

For nanotube:

$$W = U^b + \frac{4\sqrt{3}}{3}\frac{U^s}{t}, \tag{2.15}$$

For nanowire:

$$W = U^b + \frac{4\sqrt{3}}{3}\frac{U^s}{R} \tag{2.16}$$

Comparing Eqs. (2.15) with (2.16), we can observe that the geometric parameter determining the size dependency has changed from the radius $R$ for the nanowire to the wall thickness $t$ for the nanotube, which is consistent with the results demonstrated in the MDS (see Fig. 2.6d–f).

Following Huang and Yu (2006), the internal surface energy density can be written as

$$U^s(\lambda_\alpha, E_i) = U^s(0, 0) + \sigma_\alpha^0 \lambda_\alpha + \frac{1}{2} c_{\alpha\beta}^s \lambda_\alpha \lambda_\beta + D_i^0 E_i + \frac{1}{2} k_{ij}^s E_i E_j + e_{\alpha k}^s \lambda_\alpha E_k \quad (2.17)$$

where $\sigma_\alpha^0$ and $D_i^0$ can be termed as the surface stress and the surface electric displacement without applying strain and electric field, respectively; $c_{\alpha\beta}^s$, $k_{ij}^s$, and $e_{\alpha k}^s$, respectively, can be defined as the surface stiffness tensor, surface dielectric tensor, and surface piezoelectric tensor; and $\lambda_\alpha$ and $E_i$ are the strain and electric field vectors, respectively. After substituting Eq. (2.13) into Eqs. (2.15) and (2.16) and considering $c_{33} = \partial^2 W / \partial \lambda_3^2$ (Xu and Pan 2006), $e_{33} = \partial^2 W / (\partial \lambda_3 \partial E_3)$ (Dai et al. 2010), and $k_{33} = \partial^2 W / \partial E_3^2$ (Zhang 2014), we can obtain the equivalent material properties of the nanotube and nanowire from the CS model as follows:

$$\rho_{33} = \rho_{33}^b + \frac{4\sqrt{3}}{3} \frac{\rho_{33}^s}{\varsigma} \quad (2.18)$$

where $\rho_{33}^b$ and $\rho_{33}^s$ are the bulk and surface elastic constant, piezoelectric coefficient, or relative dielectric constant with $\rho \in (c, e, \varepsilon)$ and $\varsigma = t$ for the nanotube and $\varsigma = R$ for the nanowire. According to Eq. (2.14), a linear curve fitting to the data was used in the MDS depicted in Fig. 2.6d–f. Following that, we were able to present the bulk elastic constant $c_{33}^b$, the piezoelectric coefficient $e_{33}^b$, and the relative dielectric constant $\varepsilon_{33}^b$ in Fig. 2.6d–f (the values at $1/t = 0$ or $1/R = 0$). It is to be noted that the respective bulk values $c_{33}^b$, $e_{33}^b$, and $\varepsilon_{33}^b$ obtained from the present MDS-based CS model are ~319 GPa, ~0.748 C/m², and ~8.8, respectively, and are in good agreement with the experimental and ab initio findings ($c_{33}^b =$ 311 GPa, $e_{33}^b = 0.73$ C/m², and $\varepsilon_{33}^b = 9.7$, respectively) (reported in Levinshtein et al. 2001; Schwarz and Khachaturyan 1997; Bernardini and Fiorentini 1997). Moreover, the results in Fig. 2.6d–f (solid lines) of the present CS model are applicable to large-scale structure, where MDS are not feasible.

### 2.5.1.3 Piezoelectric Potential in GaN Nanotubes

In this section, the material properties measured in Sect. 2.5.1.1 are employed to study the piezoelectric potential generated in GaN nanotubes under compression. Here, as shown in Fig. 2.8, a GaN nanotube is fixed and grounded at the substrate. Then, an axial force $F$ is applied to the free surface of the nanotube to produce the piezoelectric polarization in the GaN nanotube. Theoretically, to obtain the piezoelectric potential, one needs to solve the following constitutive relations for GaN nanotubes (Zhang 2014):
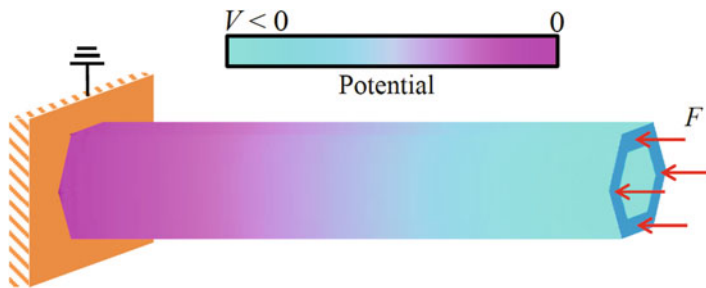
**Fig. 2.8** Piezoelectric potential distribution of a GaN nanotube subjected to the uniaxial compression (Zhang and Meguid 2015a)

$$\sigma_\alpha = c_{\alpha\beta}\lambda_\beta - e_{\alpha k}E_k \qquad (2.19)$$

$$D_i = e_{i\beta}\lambda_\beta + k_{ik}E_k \qquad (2.20)$$

where $c_{\alpha\beta}$, $e_{\alpha k}$, and $k_{ik}$ are the linear elastic constant, the piezoelectric coefficient, and the dielectric constant, respectively. $D_i$ and $\sigma_\alpha$ are the electric displacement and the stress vectors, respectively. Incorporating constitutive Eqs. (2.19) and (2.20) with the equilibrium equation, geometrical compatibility equation, and Gauss equation in Gao and Wang (2007), we have calculated the piezoelectric potential in the deformed nanotube from the finite element method (FEM). In the present study, the FEM calculation was carried out using the commercial software ANSYS. In this process, the SOLID5 element was selected to describe the piezoelectric nanotubes, and 12,000 elements were chosen after conducting element convergence analysis. The electric potential distribution in a deformed GaN nanotube obtained from the FEM calculation is plotted in Fig. 2.8. It is found that when a compression force is uniformly applied on the free surface of the nanotube, it creates a negative potential between the nanotubes and the substrate. A similar FEM calculation was also conducted to the nanowire to develop its piezoelectric potential. The obtained electric potential distribution of nanowires is found to be comparable to nanotubes, where the potential drops linearly only along the length direction.

To quantitatively evaluate the difference in the piezoelectric potential between nanotubes and nanowires, we have normalized the potential $V$ of the nanotubes by the potential $V_0$ of the nanowires to be the ratio $\alpha$. Such a piezoelectric potential ratio is then calculated in Fig. 2.9 (shown in solid squares) as a function of the wall thickness-to-radius ratio, $t/R$, of the nanotube. Here, the nanotubes and nanowires are assumed to have the same length (30 nm) and radius (3.5 nm) and are subjected to the same force (10 nN). It can be seen from Fig. 2.9 that $\alpha$ increases from 1.34 to 10.27 as $t/R$ decreases from 0.71 to 0.29. In other words, the piezoelectric potential generated in the nanotubes can be up to over nine times greater than that in the nanowires even though they have the same radii. Based on this observation, we can conclude that the nanotubes, especially those with thin wall thickness, can generate much higher piezoelectric potential than their nanowire counterparts. Thus,
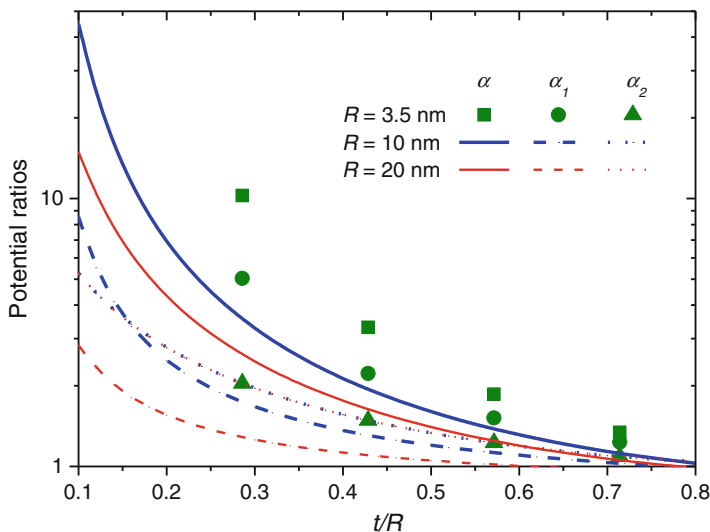
**Fig. 2.9** Piezoelectric potential ratios $\alpha$, $\alpha_1$, and $\alpha_2$ as a function of the wall thickness-to-radius ratio, $t/R$, of the GaN nanotubes with various radii $R$ (Zhang and Meguid 2015a)

compared with its mostly used nanowire counterpart, the nanotube can be considered as a better candidate for building piezotronic nanodevices in terms of its piezoelectric potential generation.

In principle, the difference between the nanowires and nanotubes may originate from their different material properties (see Fig. 2.6d–f) and geometrical properties (different cross sections). To better quantitatively understand the influence of these two factors, we have focused our attention to the following two piezoelectric potential ratios, $\alpha_1 = V_1/V_0$ and $\alpha_2 = V_2/V_0$. Here $V_1$ is the piezoelectric potential calculated based on the nanotube's material properties and the nanowire's geometrical properties, and $V_2$ is the piezoelectric potential obtained based on the nanotube's geometrical properties and the nanowire's material properties. Thus, $\alpha_1$ and $\alpha_2$ measure the contribution of material and geometrical properties of the nanotubes, respectively. The results of $\alpha_1$ (solid circles) and $\alpha_2$ (solid triangles) are plotted in Fig. 2.9 for the nanotubes with $R = 3.5$ nm and $t/R$ decreasing from 0.71 to 0.29. This figure illustrates that the different material and geometrical properties of nanotubes, compared to nanowires, enhance the piezoelectric potential of nanotubes, and this effect becomes more significant for the nanotubes with smaller $t/R$. Moreover, from Fig. 2.9, we can also observe that the resultant effect of the material and geometrical properties is much stronger than their individual effect. For example, the resultant influence ($\alpha$) from the material and geometrical properties can enhance the piezoelectric potential of nanotubes with $t/R = 0.29$ by nine times. However, the influence of the material ($\alpha_1$) properties increases the piezoelectric potential by 400 %, while the influence of the geometrical properties ($\alpha_2$) increases the piezoelectric potential by 108 %. Thus, it is of interest to examine how these two factors influence the resultant potential. In what follows, we will provide

an analytical expression of the piezoelectric potential of GaN nanotubes/nanowires under compression.

Suppose an axial force $F$ is applied on the GaN nanotube/nanowire, it will produce a uniform uniaxial strain since $\lambda_3 = -F/(c_{33}S)$. Under this uniaxial compressive strain, the wurtzite GaN cell will be deformed so that a bound charge will be generated at both ends of the structure, thus creating a dipole-like piezoelectric potential along the $c$-axis $x_3$. Due to the piezoelectric effect, the strain produces a polarization field, $P_3 = e_{33}\lambda_3$. It is known that the lateral and the free surfaces are constrained to have zero surface charge when the base of the nanotube or nanowire is connected to the ground and is at the reference potential. Under this condition, the piezoelectric potential is constant along the cross-sectional area (see Fig. 2.8), and its trend along the $c$-axis can be obtained by solving the 1D Poisson's equation (Romano et al. 2011): $\partial(k_{33}\partial\varphi/\partial x_3 - P_3)/\partial x_3 = 0$. This equation gives a linear potential profile, $\varphi = P_3 x_3/k_{33}$, where the conditions $E_3(x_3 = L) = -P_3/k_{33}$ and $\varphi(x_3 = 0) = 0$ have been used. The piezoelectric potential is therefore

$$V = \varphi(L) = -F\frac{e_{33}}{c_{33}k_0 k_{33}}\frac{L}{S} \qquad (2.21)$$

From Eq. (2.17), we can observe that the resultant influence of the material properties and geometrical properties can be considered as the product of their individual effect, i.e., $\alpha = \alpha_1 \cdot \alpha_2$.

In addition, Eq. (2.17) also provides a convenient way to predict the piezoelectric potential of a relatively large nanotube/nanowire by incorporating the CS model (see Eq. (2.14)) into it. Using this technique, we are able to calculate the piezoelectric potential ratios, $\alpha$, $\alpha_1$, and $\alpha_2$, for relatively large nanotubes, e.g., $R = 10$ and 20 nm. The results are plotted as a function of their $t/R$ ratios in Fig. 2.9 (shown by lines). This figure demonstrates that $\alpha_2$ is independent of $R$ and is only determined by the ratio, $t/R$. However, $\alpha_1$ is found to depend on both the ratio $t/R$ and the radius $R$. Specifically, $\alpha_1$ decreases with increasing $R$ and almost vanishes ($\alpha_1 \approx 1$) when $R > 135$ nm even for nanotube with extremely small wall thickness-to-radius ratio, e.g., $t/R = 0.1$. This observed $R$-dependent $\alpha_1$ and $R$-independent $\alpha_2$ further lead to a reduction in $\alpha$ with increasing $R$ as it finally approaches $\alpha_2$ when $R$ is relatively large, i.e., $R > 135$ nm. In addition, we can also observe from this figure that the contribution of the material properties (measured by $\alpha_1$) is stronger than that of the geometrical properties (measured by $\alpha_2$) for a relatively small radius of nanotube, e.g., $R = 3.5$ nm. However, due to the $R$-dependent $\alpha_1$ and $R$-independent $\alpha_2$, the contribution of the material properties is negligible compared to the geometrical properties when a relatively large nanotube is considered, e.g., $R = 20$ nm.

Finally, it is worth mentioning that the present calculation (Figs. 2.8 and 2.9, and Eq. (2.17)) is based on Lippmann theory, since we assume that there are no free charge carriers and the whole system is isolated. However, according to recent studies, the piezoelectric potential in a strained GaN nanostructure would be screened by the free charge carriers, since the as-grown GaN nanostructure always shows an n-type semiconducting behavior (Gao and Wang 2009; Romano

et al. 2011; Araneo et al. 2012). In order to overcome this screening effect, the idea of controlling the screening effect by imposing external surface charges on the nanowire/nanotube system has recently been invalidated theoretically and experimentally (Kim et al. 2012; Sohn et al. 2013). Existing numerical simulations reveal that this surface functionalization can fully deplete the free carriers (electrons) and make the piezoelectric potential of nanowires/nanotubes recover to their intrinsic case (Kim et al. 2012; Sohn et al. 2013). In addition, the numerical results also indicate that the full coverage of surface charges surrounding the nanotubes increases the piezoelectric output potential exponentially within a relatively smaller range of charge density compared to the case of nanowires for a typical donor concentration (Kim et al. 2012). This efficient surface functionalization of nanotubes could be another advantage of GaN nanotubes serving as a building block of piezotronic nanodevices, especially the nanogenerators compared with their mostly used nanowire counterparts.

### 2.5.2 Piezoelectric Effect on the Intrinsic Dissipation in Oscillating GaN Nanobelts

In this section, classical MDS have been employed to study the piezoelectric effect on the dynamic response of GaN nanobelts (see Fig. 2.10). Special attention was paid to the piezoelectric effect on the intrinsic energy dissipation of such vibrating
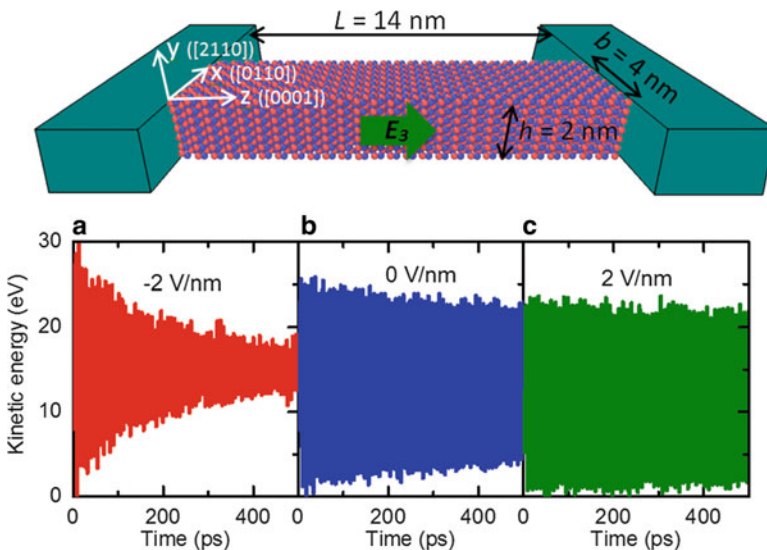


**Fig. 2.10** Top: A schematic of a doubly clamped GaN nanobelt resonator subjected to an electric field $E_3$. Here $L$, $b$, and $h$ are the respective length, width, and thickness of the nanobelt. Bottom: kinetic energy time history of the vibrating nanobelts under (**a**) $E_3 = -2$ V/nm, (**b**) no electric field ($E_3 = 0$ V/nm), and (**c**) $E_3 = 2$ V/nm (Zhang and Meguid 2015b)

GaN nanobelts, since the intrinsic energy loss sets a fundamental limit for the performance of nanodevices (Imboden and Mohanty 2014). In the present study, we considered the most common GaN nanobelts (Yu et al. 2012) whose growth direction is the $c$-axis [0001] with the top surface being [2110] and the side surface being [0110], as shown in Fig. 2.10. In this figure, the $x$-, $y$-, and $z$-axes are, respectively, taken along the [0110], [2110], and [0001] directions. The nanobelts studied here have a dimension of 14 nm $\times$ 4 nm $\times$ 2 nm. The interactions between Ga-Ga, N-N, and Ga-N were described by the SW potential (see Eqs. (2.11)–(2.13)). After obtaining the energy-minimized configuration of GaN nanobelts from the conjugate gradient method, our simulation was conducted using the following four steps. First, the initial configuration was relaxed at a specified temperature ranging from 10 to 300 K to reach its equilibrium state in 100 ps. Here, the NVT ensemble (constant number of particles, volume, and temperature) was employed to update the positions and velocities of the atoms after each time step using a Nosé-Hoover temperature thermostat (Nosé 1984). Second, to simulate the piezoelectric effect, the two ends of the relaxed nanobelt were fixed, and an electric field $E_3$ was applied along the axial direction (see Fig. 2.10), which produces an external force $f_i = q_i E_3$ on ion $i$, where $q_i$ is the charge of ion $i$. Subsequently, another relaxation with 100 ps was utilized to get the new equilibrium state. Third, after the second thermal equilibration, a point bending force was applied along the $y$-axis at the midpoint of a nanobelt to deflect it to a certain displacement, which is less than 2 % of the nanobelt length to avoid the influence of the geometric nonlinearity. Fourth, this bending force was removed, and the vibration of the nanobelt was then achieved under a constant energy (NVE) ensemble.

In Fig. 2.10a–c, we illustrate the kinetic energy time history of the vibrating nanobelts at room temperature (300 K) under different electric fields: $E_3 = -2$ V/nm in Fig. 2.10a, no electric field applied ($E_3 = 0$ V/nm) in Fig. 2.10b, and $E_3 = 2$ V/nm in Fig. 2.10c. It is worth mentioning that in Fig. 2.10a–c the total kinetic energy $E_k$ is composed of two parts: one is the external kinetic energy for the flexural mode $E_{ek}$ and the other is the internal kinetic energy $E_{ik}$ due to thermal vibrations. The oscillation in the kinetic energy reflects the vibration of nanobelts. Specifically, the kinetic energy vibrates at a frequency of $2f$, where $f$ is the natural frequency of the flexural mode of the nanobelts.

After applying the fast Fourier transform to the obtained kinetic energy time history in Fig. 2.10a–c, we obtain their corresponding frequency spectrum in Fig. 2.11a. From this figure we can see that the frequency of the nanobelts is shifted by the applied electric field through the piezoelectric effect. Similar piezoelectric effect-induced frequency shift phenomenon was also observed in recent experiments and treated as a novel method to tune the frequency of nanoelectromechanical system resonators (Masmanidis et al. 2007). In Fig. 2.11b, we plot the frequency $f$ and frequency shift $\Delta f$ of the nanobelts as a function of the electric field strength. It is observed that the resonant frequency shifts upward as the negative electric field is increased, while it shifts downward with increasing positive electric field. To explain this resonant frequency shift phenomenon, we show the distribution of the atomic
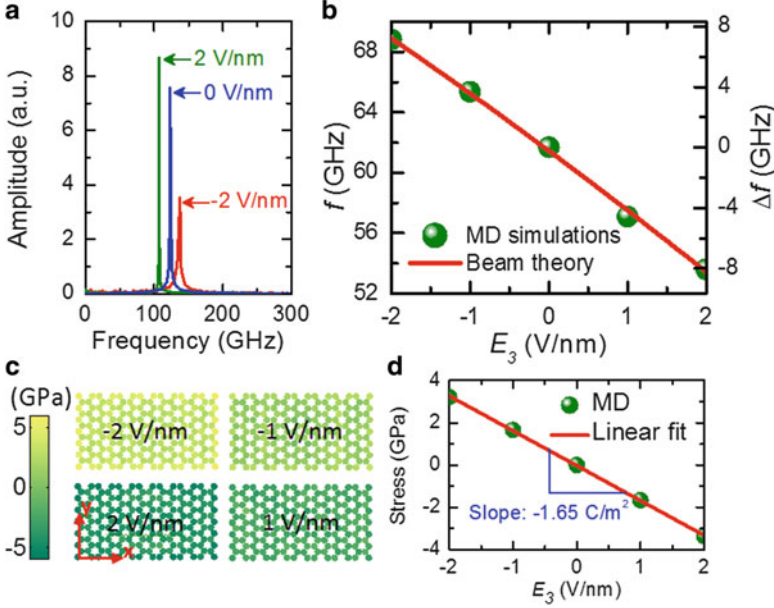
**Fig. 2.11** (**a**) Fast Fourier transform of the kinetic energy time history. (**b**) The resonant frequency $f$ and frequency shift $\Delta f$ as a function of the electric field strength $E_3$. (**c**) Distribution of the normal stress in the cross section of nanobelts subjected to different electric fields. (**d**) The average normal stress as a function of $E_3$ (Zhang and Meguid 2015b)

level stress on the cross section of GaN nanobelts subjected to different electric fields in Fig. 2.11c. We can observe from this figure that due to the piezoelectric effect, a positive stress is generated in the nanobelt by a negative electric field, and thus, according to the classical beam theory (Olsson 2010), it increases the frequency of the nanobelt. On the contrary, a negative stress is produced by a positive electric field, leading to a reduction in the frequency. In addition, according to the classical piezoelectric theory (Zhang 2014; Zhang and Meguid 2015a, b), the stress $\sigma$ in the nanobelt due to the piezoelectric effect is $\sigma = -e_{33}E_3$, where $e_{33}$ is the piezoelectric coefficient. In Fig. 2.11d, we fit this expression to the results obtained from our MDS. After curve fitting the results, we obtain $e_{33} = 1.65$ C/m$^2$, which closely agrees with the predicted values for GaN nanowires with the same cross-sectional size using first-principle calculations (Hoang et al. 2013).

Moreover, analogous to the experimental observation (Masmanidis et al. 2007), an almost linear relationship between the frequency shift and the electric field strength is also observed in the present MDS results (see Fig. 2.11b). To shed light on this observation, we resort to the classical piezoelectric and Euler beam theories, which give the resonant frequency $f$ as

$$f = f_0 \sqrt{1 - \frac{E_3 e_{33} A L^2}{4\pi^2 EI}} \tag{2.22}$$

where $A$ is the cross-sectional area, $I$ is the second moment of area, $L$ is the length of the nanobelt, $E$ is Young's modulus, and $f_0 = 3.56\sqrt{EI/(\rho AL^4)}$ ($\rho$ being the mass density) is the frequency of the nanobelt without piezoelectric effect. Under small electrical perturbations, the frequency shift obtained from Eq. (2.18) is $\Delta f = -f_0 E_3 e_{33} AL^2/(8\pi^2 EI)$. This expression shows a linear relationship between $\Delta f$ and $E_3$, which agrees with our MDS results (see Fig. 2.11b). In addition, we obtain the piezoelectric coefficient of the present GaN nanobelts as $e_{33} = 1.7$ C/m$^2$ by fitting the $f$ - $E_3$ curve in Fig. 2.11b with Eq. (2.18). The obtained piezoelectric coefficient is consistent with the value calculated by above direct measurements (Fig. 2.11d).

Next, we will turn our attention to the energy dissipation (the quality factor) of the GaN nanobelt resonator. In Fig. 2.10a–c, the decay of the oscillation amplitude in the kinetic energy represents the energy dissipation in the nanobelt resonators. Assuming that the quality factor $Q$ is constant during vibration, i.e., after $n$ vibration cycles, the maximum external kinetic energy $E_{ek}(n)$ is related to the initial external kinetic energy $E_{ek}(0)$ by the relation $E_{ek}(n) = E_{ek}(0)(1 - 2\pi/Q)^n$ (Jiang et al. 2004). This expression is used in the present work to determine the quality factors of the nanobelt resonators based on their kinetic energy time history (Fig. 2.10a–c). In addition, comparing Fig. 2.10a–c, we can observe that the nanobelt resonator that is subjected to a negative electric field (Fig. 2.10a) demonstrates considerable higher energy dissipation than its counterpart without an electric field (Fig. 2.10b). On the contrary, the nanobelt resonator subjected to a positive electric field (Fig. 2.10c) holds much lower energy dissipation. These results suggest that the piezoelectric effect can greatly influence the energy dissipation and thus the quality factor of the nanobelt resonators. Indeed, we calculated $Q$ of a nanobelt resonator as a function of the electric field strength $E_3$ in Fig. 2.12a. It can be seen from Fig. 2.12a that $Q$ is increased by up to 12 times as $E_3$ increases from $-2$ to $2$ V/nm. In other words, a negative electric field significantly decreases the quality factor, while a positive one increases it. This result suggests that applying a negative electric field can mitigate the intrinsic loss of GaN nanobelt resonators via their piezoelectric effect.

To provide some possible explanation to the above observed phenomenon, we will present a brief discussion based on the classical theory of energy dissipation at the nanoscale. Among various sources of the energy dissipation, it is believed that at relatively high temperature ($>100$ K), the thermoelastic dissipation is the dominant mechanism for a nanobeam oscillator involving bending deformation (Jiang et al. 2004). Based on Zener's work on rectangular reeds (Li et al. 2010), the thermoelastic dissipation in the flexural mode of the present nanobelt can be approximated by (Jiang et al. 2004)

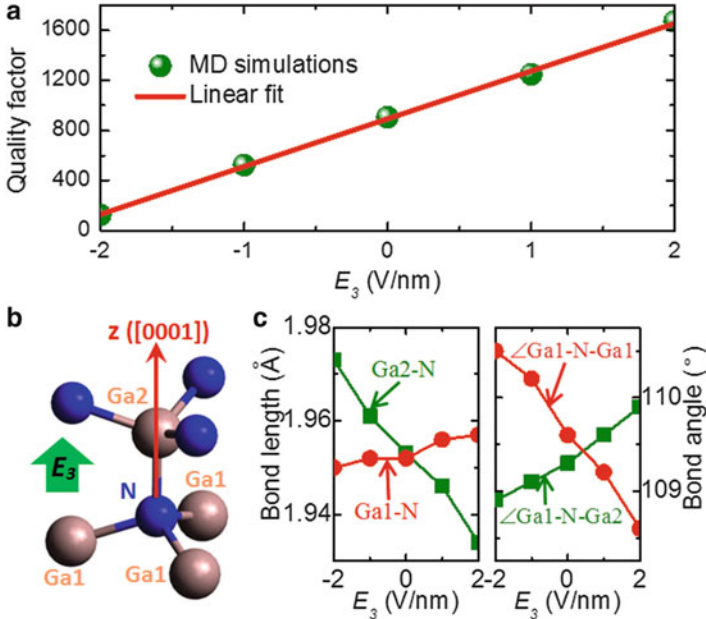$$\frac{1}{Q} = \frac{2E\alpha^2 h^2}{\pi k} Tf \qquad (2.23)$$

**Fig. 2.12** (**a**) The quality factor as a function of the electric field strength $E_3$. (**b**) The bond configuration of the wurtzite GaN. (**c**) The evolution of bond length and bond angle of the wurtzite GaN subjected to $E_3$ (Zhang and Meguid 2015b)

where $\alpha$ is the coefficient of thermal expansion, $k$ is the thermal conductivity, $h$ is the thickness of the nanobelt, and $T$ is the temperature. Equation (2.19) shows that the quality factor $Q$ increases with the decrease in the resonant frequency $f$ since $Q \propto 1/f$. This trend is consistent with our MDS results, where a negative $E_3$ increases $f$ but reduces $Q$ and a positive $E_3$ decreases $f$ but improves $Q$. In addition, it is also expected from Eq. (2.19) that the relative change in $1/Q$ should be close to the relative change in $f$. Nevertheless, from Figs. 2.11b to 2.12a, we can observe that $1/Q$ can be reduced by up to 92 % as $E_3$ increases from $-2$ to 2 V/nm. However, in this process $f$ is found to be decreased by only 22 %. In other words, if compared with $f$, the change of $Q$ is more sensitive to the change of the applied electric field. This observation implies that the figure of merit $(f \cdot Q)$ of the nanobelt resonator can be efficiently tuned by applying an electric field, and specifically a negative electric field can improve the performance of the resonator. On the other hand, the more sensitive $Q$ (compared with $f$) to the electric field also suggests that the piezoelectric effect may influence the thermoelastic dissipation and the quality factor through some other factors, including $f$. To shed some light on this issue, let us examine the atomic details of the wurtzite GaN subjected to an electric field, whose atomic structure is illustrated in Fig. 2.12b. For this purpose, we measured the variation of bond lengths and angles with different applied electric fields and plotted the measured results in Fig. 2.12c. It can be seen from Fig. 2.12c that due to the
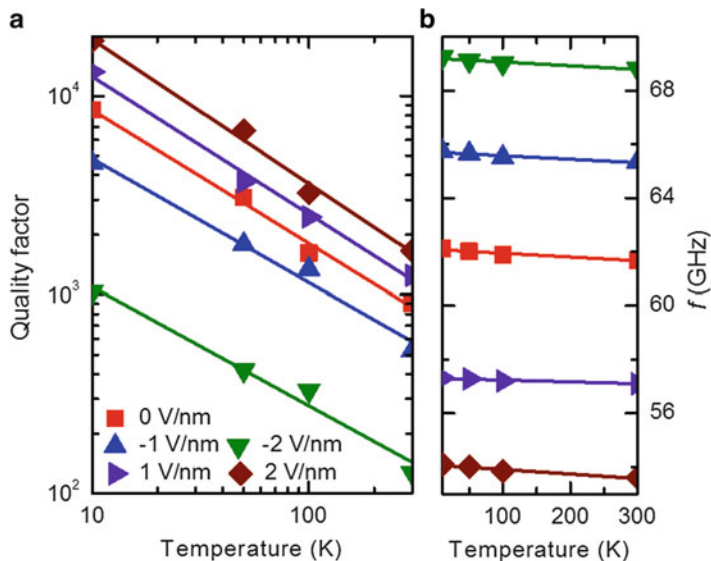
**Fig. 2.13** (**a**) The quality factor and (**b**) the resonant frequency $f$ as a function of the temperature for GaN nanobelts subjected to different electric fields (Zhang and Meguid 2015b)

piezoelectric effect, the bond lengths and angles of wurtzite GaN significantly vary with the changing electric field. It has been proven from previous studies on carbon nanotubes (Li et al. 2010), graphene sheets (Li et al. 2010), and semiconductor nanowires (Li et al. 2010) that the varied bond lengths and angles of nanostructures greatly shift their phonon spectra and thus significantly influence their thermal conductivity. Thus, based on this discussion together with Eq. (2.19), we can conclude that the changed thermal conductivity $k$ of GaN nanobelts due to the piezoelectric effect can be regarded as another possible explanation for the electric field-dependent quality factor detected in the present study.

Finally, we will study the dependence of the dynamic behaviors ($Q$ and $f$) on the temperature $T$. We display $Q$ of nanobelts subjected to various electric fields against $T$ in Fig. 2.13a. From this figure we can deduce that $Q$ increases exponentially with decreasing $T$ and can be described by the following relation, $Q \propto 1/T^{\beta}$, where the thermoelastic damping exponent $\beta$ is in the range 0.59–0.72, and depends on the electric field strength. Such deduction relationship of the quality factor with increasing temperature deviates from the $1/T$ dependence obtained from the classical description of thermoelastic loss for bulk materials (Eq. (2.19)). This discrepancy is attributed to a surface effect, which results in dynamic behaviors of the surface layer of the nanobelt that is distinctly different from its bulk counterpart (Zhang et al. 2012b). In addition, although the initial temperatures are fixed in the simulations, a small raise of the temperature is still unavoidable because of the nature of the simulations in the micro-canonical ensemble. This slight temperature increase could be another explanation for the above observed discrepancy.

It is noted here that $\beta = 0.67$ for GaN nanobelts without an applied electric field is close to that of 0.7 as obtained from MDS of silicon nanowires (Georgakaki et al. 2014). Moreover, $\beta$ is found to significantly depend on the electric field strength, $E_3$. This $E_3$-dependent $\beta$ can be attributed to the pyroelectric character of the wurtzite GaN crystal, which makes the piezoelectric effect of GaN nanobelts temperature dependent (Zhang et al. 2013; Zhang and Meguid 2015a). We further determined the influence of the temperature on the resonant frequency of GaN nanobelts. Owing to the so-called thermal-softening effect on the elastic properties and/or the pyroelectric effect, $f$ is found to decrease with increasing $T$ (Fig. 2.13b). However, the effect of $T$ on $f$ almost can be ignored, since $f$ is reduced by no more than 1 % when $T$ increases from 10 to 300 K. Similar negligible influence of temperature on the resonant frequency was also observed in a recent experimental study of GaN nanowire resonators (Montague et al. 2012).

## 2.6 Conclusion Remarks

Piezoelectric response in a nanoscale world has attracted considerable attention in recent research. Effort has been made to characterize the piezoelectricity of PNs in different configurations. Experimental techniques were used for synthesized PNs of the feature size tens to hundreds of nanometers, while the atomistic simulations are focused on small PNs of the feature size 0.5–10 nm. Due to unknown physical mechanisms, strong or extreme piezoelectric response was reported for ZnO PNs, characterized by the EPCs orders of magnitude greater than the bulk values. In particular the EPCs at the nanoscale are not constants but vary significantly with the geometric size of PNs. On the other hand, large discrepancy is found among the existing studies in measuring the values of EPCs and predicting their size dependence.

In addition, various mechanisms have been proposed as possible physical origins of unique piezoelectric response at the nanoscale, such as the quantum effects, single or polycrystallinity, the density of defects, the free relaxation of surface atoms, and the piezoelectricity of the surface layers. The effect of individual factor may vary drastically in different cases, e.g., length scales. Specifically, the theoretical framework of the surface piezoelectricity has been established and was found to be in good agreement with some atomistic simulations. Thus, surface piezoelectricity can be accepted as a major factor that determines the magnitudes and behavior of the EPCs of PNs, at least, in some cases. Nevertheless, it still remains a challenge to formulate a universal theoretical framework that is able to achieve physical insights into the scattering of the obtained results.

Moreover, based on the structural models accounting for the effect of the surface piezoelectricity, two types of EPCs of PNs are derived for the first time characterizing the relation of an electric field to the initial stress and the contribution of piezoelectricity to EEM. Both of them are found to vary with not only the geometric size of PNs but also the deformation experienced by the PNs.

Finally, the influence of the nanoscale piezoelectricity on the mechanical responses (statics and dynamics) of piezoelectric nanostructures was also discussed. It is found that at the nanoscale, the surface piezoelectricity can enhance the piezoelectric potential of nanostructures when they are subjected to a static deformation. In addition, the intrinsic loss of oscillating piezoelectric nanostructure can be mitigated through the piezoelectric effect at the nanoscale.

# References

Araneo, R., Lovat, G., Burghignoli, P., Falconi, C.: Piezo-semiconductive quasi-1D nanodevices with or without anti-symmetry. Adv. Mater. **24**, 4719–4724 (2012)

Assadi, A., Farshi, B.: Vibration characteristics of circular nanoplates. J. Appl. Phys. **108**, 074312 (2010)

Assadi, A., Farshi, B., Alinia-Ziazi, A.: Size dependent dynamic analysis of nanoplates. J. Appl. Phys. **107**, 124310 (2010)

Bdikin, I.K., Gracio, J., Ayouchi, R., Schwarz, R., Kholkin, A.L.: Local piezoelectric properties of ZnO thin films prepared by RF-plasma-assisted pulsed-laser deposition method. Nanotechnology **21**, 235703 (2010)

Bere, A., Serra, A.: On the atomic structures, mobility and interactions of extended defects in GaN: dislocations, tilt and twin boundaries. Philos. Mag. **86**, 2159–2192 (2006)

Bernardini, F., Fiorentini, V.: Spontaneous polarization and piezoelectric constants of III-V nitrides. Phys. Rev. B **56**, R10024 (1997)

Chen, C.Q., Shi, Y., Zhang, Y.S., Zhu, J., Yan, Y.J.: Size dependence of Young's modulus in ZnO nanowires. Phys. Rev. Lett. **96**, 075505 (2006)

Dai, S.X., Dunn, M.L., Park, H.S.: Piezoelectric constants for ZnO calculated using classical polarizable core-shell potentials. Nanotechnology **21**, 445707 (2010)

Dai, S.X., Gharbi, M., Sharma, P., Park, H.S.: Surface piezoelectricity: size effects in nanostructures and the emergence of piezoelectricity in non-piezoelectric materials. J. Appl. Phys. **110**, 104305 (2011)

Dunn, S.: Strain behaviour of thin film PZT (30/70) examined through piezoforce microscopy (P-AFM). J. Appl. Phys. **94**, 5964–5968 (2003)

Ebbesen, T.W., Ajayan, P.M.: Large-scale synthesis of carbon nanotubes. Nature **358**, 220–222 (1992)

Espinosa, H.D., Bernal, R.A., Minary-Jolandan, M.: A review of mechanical and electromechanical properties of piezoelectric nanowires. Adv. Mater. **24**, 4656–4675 (2012)

Fan, H.J., Lee, W., Hauschild, R., Alexe, M., Le Rhun, G., Scholz, R., Dadgar, A., Nielsch, K., Kalt, H., Krost, A., Zacharias, M., Gosele, U.: Template-assisted large-scale ordered arrays of ZnO pillars for optical and piezoelectric applications. Small **2**, 561–568 (2006)

Fang, X.Q., Liu, J.X., Gupta, V.: Fundamental formulations and recent achievements in piezoelectric nano-structures: a review. Nanoscale **5**, 1716–1726 (2013)

Faucher, M., Grimbert, B., Cordier, Y., Baron, N., Wilk, A., Lahreche, H., Bove, P., François, M., Tilmant, P., Gehin, T., Legrand, C., Werquin, M., Buchaillot, L., Gaquière, C., Théron, D.: Influence of carrier concentration on piezoelectric potential in a bent ZnO nanorod. Appl. Phys. Lett. **94**, 233506 (2009)

Gao, Y., Wang, Z.L.: Electrostatic potential in a bent piezoelectric nanowire. The fundamental theory of nanogenerator and nanopiezotronics. Nano Lett. **7**, 2499–2505 (2007)

Gao, Y., Wang, Z.L.: Equilibrium potential of free charge carriers in a bent piezoelectric semiconductive nanowire. Nano Lett. **9**, 1103–1110 (2009)

Geim, A.K., Novoselov, K.S.: The rise of graphene. Nat. Mater. **6**, 183–191 (2007)

Georgakaki, D., Ziogos, O.G., Polatoglou, H.M.: Vibrational and mechanical properties of Si/Ge nanowires as resonators: a molecular dynamics study. Phys. Status Solidi A **211**, 267–276 (2014)

Han, W.Q., Redlich, P., Ernst, F., Ruhle, M.: Synthesis of GaN-carbon composite nanotubes and GaN nanorods by arc discharge in nitrogen atmosphere. Appl. Phys. Lett. **76**, 652–654 (2000)

He, M.R., Shi, Y., Zhou, W., Chen, J.W., Yan, Y.J., Zhu, J.: Diameter dependence of modulus in zinc oxide nanowires and the effect of loading mode: in situ experiments and universal core-shell approach. Appl. Phys. Lett. **95**, 091912 (2009)

Hoang, M.T., Yvonnet, J., Mitrushchenkov, A., Chambaud, G.: First-principles based multiscale model of piezoelectric nanowires with surface effects. J. Appl. Phys. **113**, 014309 (2013)

Huang, G.Y., Yu, S.W.: Effect of surface piezoelectricity on the electromechanical behaviour of a piezoelectric ring. Phys. Status Solidi B **243**, R22–R24 (2006)

Huang, Y., Wu, J., Hwang, K.C.: Thickness of graphene and single-wall carbon nanotubes. Phys. Rev. B **74**, 245413 (2006)

Iijima, S.: Helical microtubules of graphitic carbon. Nature **354**, 56–58 (1991)

Imboden, M., Mohanty, P.: Dissipation in nanoelectromechanical systems. Phys. Rep. **534**, 89–146 (2014)

Jiang, H., Yu, M.F., Liu, B., Huang, Y.: Intrinsic energy loss mechanisms in a cantilevered carbon nanotube beam oscillator. Phys. Rev. Lett. **93**, 185501 (2004)

Kim, S.M., Kim, H., Nam, Y., Kim, S.: Effects of external surface charges on the enhanced piezoelectric potential of ZnO and AlN nanowires and nanotubes. AIP Adv. **2**, 042174 (2012)

Kroto, H.W., Heath, J.R., O'Brien, S.C., Curl, R.F., Smalley, R.E.: C60: Buckminsterfullerene. Nature **318**, 162–163 (1985)

Levinshtein, M.E., Rumyantsev, S.L., Shur, M.S.: Properties of advanced semiconductor materials: GaN, AlN, InN, BN, SiC, SiGe. Wiley, New York (2001)

Li, C., Guo, W.L., Kong, Y., Gao, H.J.: Size-dependent piezoelectricity in zinc oxide nanofilms from first-principles calculations. Appl. Phys. Lett. **90**, 033108 (2007)

Li, X.B., Maute, K., Dunn, M.L., Yang, R.G.: Strain effects on the thermal conductivity of nanostructures. Phys. Rev. B **81**, 245318 (2010)

Li, Y.H., Fang, B., Zhang, J.Z., Song, J.Z.: Surface effects on the wrinkling of piezoelectric films on compliant substrates. J. Appl. Phys. **110**, 114303 (2011)

Liu, C., Rajapakse, R.K.N.D.: Surface energy incorporated continuum models for static and dynamic response of nanoscale beams. IEEE Trans. Nanotechnol. **9**, 422–431 (2010)

Masmanidis, S.C., Karabalin, R.B., De Vlaminck, I., Borghs, G., Freeman, M.R., Roukes, M.L.: Multifunctional nanomechanical systems via tunably coupled piezoelectric actuation. Science **317**, 780–783 (2007)

Miller, R.E., Shenoy, V.B.: Size-dependent elastic properties of nanosized structural elements. Nanotechnology **11**, 139–147 (2000)

Minary-Jolandan, M., Bernal, R.A., Kuljanishvili, I., Parpoil, V., Espinosa, H.D.: Individual GaN nanowires exhibit strong piezoelectricity in 3D. Nano Lett. **12**, 970–976 (2012)

Momeni, K., Attariani, H.: Electromechanical properties of 1D ZnO nanostructures: nanopiezotronics building blocks, surface and size-scale effects. Phys. Chem. Chem. Phys. **16**, 4522–4527 (2014)

Momeni, K., Odegard, G.M., Yassar, R.S.: Finite size effect on the piezoelectric properties of ZnO nanobelts: a molecular dynamics approach. Acta Mater. **60**, 5117–5124 (2012)

Montague, J.R., Bertness, K.A., Sanford, N.A., Bright, V.M., Rogers, C.T.: Temperature-dependent mechanical-resonance frequencies and damping in ensembles of gallium nitride nanowires. Appl. Phys. Lett. **101**, 173101 (2012)

Nosé, S.: A unified formulation of the constant temperature molecular dynamics methods. J. Chem. Phys. **81**, 511–519 (1984)

Olsson, P.A.T.: Transverse resonant properties of strained gold nanowires. J. Appl. Phys. **108**, 034318 (2010)

Plimpton, S.J.: Fast parallel algorithms for short-range molecular dynamics. J. Comput. Phys. **117**, 1–19 (1995)

Romano, G., Mantini, G., Di Carlo, A., D'Amico, A., Falconi, C., Wang, Z.L.: Piezoelectric potential in vertically aligned nanowires for high output nanogenerators. Nanotechnology **22**, 465401 (2011)

Schwarz, R.B., Khachaturyan, K.: Elastic moduli of gallium nitride. Appl. Phys. Lett. **70**, 1122–1124 (1997)

Shen, S., Hu, S.: A theory of flexoelectricity with surface effect for elastic dielectrics. J. Mech. Phys. Solids **58**, 665–677 (2010)

Smith, M.B., Page, K., Siegrist, T., Redmond, P.L., Walter, E.C., Seshadri, R., Brus, L.E., Steigerwald, M.L.: Crystal structure and the paraelectric-to-ferroelectric phase transition of nanoscale BaTiO3. J. Am. Chem. Soc. **130**, 6955–6963 (2008)

Sohn, J.I., Cha, S.N., Song, B.G., Lee, S., Kim, S.M., Ku, J., Kim, H.J., Park, Y.J., Choi, B.L., Wang, Z.L., Kim, J.M., Kim, K.: Engineering of efficiency limiting free carriers and an interfacial energy barrier for an enhancing piezoelectric generation. Energ. Environ. Sci. **6**, 97–104 (2013)

Stillinger, F.H., Weber, T.A.: Computer simulation of local order in condensed phases of silicon. Phys. Rev. B **31**, 5262–5271 (1985)

Wang, Z.L.: ZnO nanowire and nanobelt platform for nanotechnology. Mater. Sci. Eng. R **64**, 33–71 (2009)

Wang, G.F., Feng, X.Q.: Timoshenko beam model for buckling and vibration of nanowires with surface effects. J. Phys. D Appl. Phys. **42**, 155411 (2009)

Wang, G.F., Feng, X.Q.: Effect of surface stresses on the vibration and buckling of piezoelectric nanowires. Europhys. Lett. **91**, 56007 (2010)

Wang, Z.G., Zu, X.T., Gao, F., Weber, W.J.: Atomistic simulation of brittle to ductile transition in GaN nanotubes. Appl. Phys. Lett. **89**, 243123 (2006a)

Wang, X.B., Song, C., Li, D.M., Geng, K.W., Zen, F., Pan, F.: The influence of different doping elements on microstructure, piezoelectric coefficient and resistivity of sputtered ZnO film. Appl. Surf. Sci. **253**, 1639–1643 (2006b)

Wang, Z.G., Zu, X.T., Yang, L., Gao, F., Weber, W.J.: Atomistic simulations of the size, orientation, and temperature dependence of tensile behavior in GaN nanowires. Phys. Rev. B **76**, 045310 (2007)

Wang, Z.G., Zu, X.T., Gao, F., Weber, W.J.: Mechanical behavior of gallium nitride nanotubes under combined tension-torsion: an atomistic simulation. J. Appl. Phys. **103**, 013505 (2008)

Xiang, H.J., Yang, J.L., Hou, J.G., Zhu, Q.S.: Piezoelectricity in ZnO nanowires: a first-principles study. Appl. Phys. Lett. **89**, 223111 (2006)

Xu, B., Pan, B.C.: The effect of atomic vacancies and grain boundaries on the mechanical proper. J. Appl. Phys. **99**, 104314 (2006)

Xu, F., Qin, Q.Q., Mishra, A., Gu, Y., Zhu, Y.: Mechanical properties of ZnO nanowires under different loading modes. Nano Res. **3**, 271–280 (2010)

Yan, Z., Jiang, L.Y.: Surface effects on the electromechanical coupling and bending behaviours of piezoelectric nanowires. J. Phys. D Appl. Phys. **44**, 075404 (2010)

Yan, Z., Jiang, L.Y.: The vibrational and buckling behaviors of piezoelectric nanobeams with surface effects. Nanotechnology **22**, 245703 (2011)

Yang, Y., Guo, W., Wang, X., Wang, Z., Qie, J., Zhang, Y.: Size dependence of dielectric constant in a single pencil-like ZnO nanowire. Nano Lett. **12**, 1919–1922 (2012)

Yao, H.Y., Yun, G.H., Bai, N.: Influence of exponentially increasing surface elasticity on the piezoelectric potential of a bent ZnO nanowire. J. Phys. D Appl. Phys. **45**, 285304 (2012)

Yu, R.M., Dong, L., Pan, C.F., Niu, S.M., Liu, H.F., Liu, W., Chua, S.J., Chi, D.Z., Wang, Z.L.: Piezotronic effect on the transport properties of GaN nanobelts for active flexible electronics. Adv. Mater. **24**, 3532–3537 (2012)

Zhang, J.: Small-scale effect on the piezoelectric potential of gallium nitride nanowires. Appl. Phys. Lett. **104**, 253110 (2014)

Zhang, J., Meguid, S.A.: On the piezoelectric potential of gallium nitride nanotubes. Nano Energ. **12**, 322–330 (2015a)

Zhang, J., Meguid, S.A.: Piezoelectric effect on the intrinsic dissipation in oscillating gallium nitride nanobelts. Europhys. Lett. **112**, 26003 (2015b)

Zhang, J., Wang, C.Y.: Vibrating piezoelectric nanofilms as sandwich nanoplates. J. Appl. Phys. **111**, 094303 (2012)

Zhang, Y.H., Hong, J.W., Liu, B., Fang, D.N.: Molecular dynamics investigations on the size-dependent ferroelectric behavior of BaTiO3 nanowires. Nanotechnology **20**, 405703 (2009)

Zhang, Y.H., Hong, J.W., Liu, B., Fang, D.N.: Strain effect on ferroelectric behaviors of BaTiO3 nanowires: a molecular dynamics study. Nanotechnology **21**, 015701 (2010)

Zhang, J., Wang, C.Y., Adhikari, S.: Surface effect on the buckling of piezoelectric nanofilms. J. Phys. D Appl. Phys. **45**, 285301 (2012a)

Zhang, J., Wang, C.Y., Chowdhury, R., Adhikari, S.: Small-scale effect on the mechanical properties of metallic nanotubes. Appl. Phys. Lett. **101**, 093109 (2012b)

Zhang, J., Wang, C.Y., Chowdhury, R., Adhikari, S.: Size-and temperature-dependent piezoelectric properties of gallium nitride nanowires. Scr. Mater. **68**, 627–630 (2013)

Zhang, J., Wang, C.Y., Bowen, C.: Piezoelectric effects and electromechanical theories at the nanoscale. Nanoscale **6**, 13314–13327 (2014)

Zhao, M.H., Wang, Z.L., Mao, S.X.: Piezoelectric characterization of individual zinc oxide nanobelt probed by piezoresponse force microscope. Nano Lett. **4**, 587–590 (2004)

Zhu, R., Wang, D.Q., Xiang, S.Q., Zhou, Z.Y., Ye, X.Y.: Piezoelectric characterization of a single zinc oxide nanowire using a nanoelectromechanical oscillator. Nanotechnology **19**, 285712 (2008)